THESIS

STUDY OF REAL-TIME SPATIAL AND TEMPORAL BEHAVIOR OF BACTERIAL BIOFILMS USING 2D IMPEDANCE SPECTROSCOPY

Submitted by

Caleb R. Begly

Department of Electrical and Computer Engineering

In partial fulfillment of the requirements

For the Degree of Master of Science

Colorado State University

Fort Collins, Colorado

Fall 2019

Master's Committee:

Advisor: Thomas W. Chen

Jesse Wilson
Adam Chicco

ABSTRACT

STUDY OF REAL-TIME SPATIAL AND TEMPORAL BEHAVIOR OF BACTERIAL BIOFILMS USING 2D IMPEDANCE SPECTROSCOPY

The study of biofilms and their effect on disease treatment, prevention, and cures has been increasing in importance in recent years. Bacterial biofilms are colony formations developed by bacteria that allow them to anchor onto a surface and survive hostile environments. The formation of harmful bacteria biofilms on some surfaces can be troublesome, particularly in the case of medical implants. The continuing rise of antibiotic resistant bacteria over the past decade had escalated the need to study and understand biofilms. This thesis presents the design of a multi-channel impedance spectroscopy instrument to allow 2D spatial and temporal evaluation of biofilm growth. The custom-designed circuits allow measurement updates once per second on the entire set of impedance sensors. The distance between the neighboring sensors is 220 micrometers, allowing real-time observation of biofilm growth. The initial results show that the proposed 2D impedance spectroscopy tool provides the needed accuracy to predict the existence of bacteria biofilm at a given sensor location. The initial results were validated using optical images with fluorescent staining.

ACKNOWLEDGEMENTS

- To collaborators Forrest Ackart and Julian Mylius for helping with designing and performing the wet lab validation, and to Randall Basaraba for providing the resources needed for the validation.
- To Daniel Ball for providing good advice and suggestions when needed, and providing motivation.
- To William Tedjo, Lang Yang, Nick Grant, and Yusra Obeidat for technical teaching, help, motivation, and suggestions.
- To Luke Schwerdtfeger for performing the fluorescent imaging, and to Stuart Tobet for providing the equipment, and helping with other research
- To Tom Chen who is an engineering inspiration to me and many others.
- To my Dad for encouraging me and developing my work ethic. Bonus Round!

Results presented in this thesis are based upon collaborative work supported by a National Science Foundation NRT Grant No. 1450032. Any opinions, findings, conclusions or recommendations expressed in this paper are those of the author(s) and do not necessarily reflect the views of the National Science Foundation.

DEDICATION

I would like to dedicate this thesis to my Mom

Martha K. Ferns

יִשָּׂא יְהוָה פָּנָיו אֵלֶיךָ, וְיָשֵׂם לְךָ שָׁלוֹם

TABLE OF CONTENTS

LIST OF TABLES

LIST OF FIGURES

Chapter 1

Introduction

The study of biofilms and their effect on disease treatment, prevention, and cures has been increasing in importance in recent years. Back in 2002, the NIH turned its sights on biofilms, stating that at the time over 80% of microbial infections were associated with biofilms in the body [1]. Among the goals were the desire to develop instruments or techniques capable of non-destructive, real-time, three dimensional monitoring of biofilms. Steady increases in antibiotic resistant bacteria deaths year-over-year, have made the study of biofilms more urgent now than in the previous two decades.

1.1 Biofilm Background

Bacterial biofilms are colony formations developed by bacteria that allow them to anchor onto a surface, and survive hostile environments. In the lifecycle of a bacteria biofilm, free floating (planktonic) bacteria anchor onto a surface and then secrete extracellular polysacharides (EPS) which form a slimy residence for the new colony to grow and thrive in, eventually reaching a mature colony size [2]. At this point, the colony will continue to release planktonic bacteria into the surrounding environment from the outer surface of the biofilm [2].

The formation of harmful bacteria biofilms on some surfaces can be troublesome, particularly in the case of medical implants. Once a biofilm forms on an implant, the biofilm will continue to harbor the infection, distributing planktonic bacteria into the surrounding environment [2]. The EPS matrix shields the cells inside from hostile environments, and limits the effect of treatments. Antibiotic treatments are generally ineffective alone because they only impact the free floating bacteria and bacteria on the very surface of the biofilm. Instead, either

high-dose, long term antibiotic treatment is needed to give the antibiotic ample opportunity to penetrate the biofilm, or the implant must be removed [1, 2].

1.2 Antibiotic Resistant Concerns

Adding to the need to study and understand biofilms is the increase in antibiotic resistant bacteria. The NIH noted in its proposal for studying biofilms that bacteria in biofilms can have higher antibiotic resistance naturally (due to EPS shielding) and they increase the likelihood of gene transfer [1]. The long, high-dose antibiotic treatments needed to get rid of, or suppress biofilms further increase the likelihood of selecting antibiotic resistant strains over the course of the treatment.

There is a general, and concerning increase in drug-resistant infections over time. Over seven hundred thousand people currently die each year from antimicrobial resistant disease, and that figure is expected to increase to ten million by 2050, finally eclipsing cancer as the number one cause of death [3]. A summary report from the UK Review on Anti-Microbial Resistance recommends reduction of unnecessary use of antibiotics, development of better diagnostics, and development of alternatives as ways to combat the increase in drug-resistant deaths [4], however there is still a need for new tools to allow studying drug-resistant strains so new treatments can be developed.

Among the causes of deaths due to bacteria, *Mycobacterium tuberculosis* (TB) stands out as a large and continuing problem. As of 2014, it accounts for 1.5 million deaths annually, and the multi drug-resistant variants of TB kill two hundred thousand people annually - 28.6% of all deaths due to anti-microbial resistant infections [4]. In this paper we use *Mycobacterium smegmatis* to validate the capabilities of our device. This was chosen because it is a common model for studying *M. tuberculosis*, although there are some limitations [5].

1.3 Current Solutions

There is already some progress in finding alternatives to antibiotics in the case of medical implants. Surface structure treatments, and novel materials can provide good alternative to the current practice of antibiotic treatment of medical implants (antibiotic catheter lock therapy and antibiotic coatings) [2]. New materials like metal - organic framework (MOF) containing substances have been shown to be effective at preventing biofilm formation of *Pseudomonas aeruginosa* without the use of antibiotics [6]. These new materials help reduce the issues of biofilm formation on new implants, but there is still a need to study biofilms for management and removal of biofilms in existing situations, or in tough cases where the biofilm forms on the surfaces of other organs. For example, some *P. aeruginosa* strains form biofilms on the surface of lung tissue [7]).

Electrochemical impedance spectroscopy (EIS) has been used as a technique for real-time monitoring of biofilms in many applications, due to its ability to measure characteristics of the biofilm without damaging the cells [8]. The technique involves applying a small stimulus voltage ($5 - 100\,\mathrm{mV_{pp}}$) to the system, and then measuring the current over a wide range of frequencies to measure the resistance between two electrodes where biofilm may grow [9–16]. By keeping the stimulus small, the system can measure the response in the pseudo-linear range, and avoid any substantial disruption to the specimen or solution [17]. Some of the promising approaches so far involve growing the biofilm on a macro electrode, and then monitoring the change in EIS [9–13].

While these approaches demonstrate how EIS can be used with good temporal resolution, developing a measurement system that has 2D spatial resolution is more challenging. A 2005 project used a combination optical and microelectrode EIS probe to get spatial information by using a motorized stage to scan the probe over the surface of a biofilm grown on a macroelectrode [18]. A similar 2013

project used a conductive atomic force microscopy (AFM) tip to perform a 2D EIS scan of the biofilm [19]. Both techniques gave good spatial resolution, but sacrificed temporal resolution[1]. In addition, moving a probe through the solution above a biofilm has the potential to disrupt the biofilm while the measurement is being taken.

To allow for measurements with high spatial resolution as well as temporal resolution, a microelectrode array can be used. A 2012 project used a 96×96 electrode array (9216 electrodes) developed using a CMOS process to measure EIS in a 2D plane [14]. It has lower spatial resolution ($\approx 17\,\mu\mathrm{m}$ versus $\approx 1\,\mu\mathrm{m}$) but potentially improves temporal resolution over the scanned modes [14, 19]. Measurements were taken using an external LCR meter, limiting the portability and volumetric density of the device compared to other designs.

Another 2D electrode array design was attempted and featured a 10x10 electrode array developed using a CMOS process [20]. The electrodes on this chip are round with a diameter of $100\,\mu\mathrm{m}$, and a pitch of $\approx 150\,\mu\mathrm{m}$ [20][2]. Similar to the other example [14], this device uses a separate reference/counter electrode so the EIS measurements are taken vertically [20]. While the spatial resolution is less than other approaches, this chip includes a built-in frequency synthesizer and readout, making it potentially more compact, however readouts from the chip were still performed using an external data acquisition card.

The above mentioned approaches used plain disk [18, 20] or disk analogue [14] microelectrodes, however interdigitated electrodes can be used to measure effects closer to the surface of the electrode. This is useful when looking at effects like biofilms bonding to the surface of the electrode. Using an width-to-gap ratio on the interdigitated electrode array of 3:4, 90% of the total electric field strength

[1]The exact reduction in temporal resolution for both papers is unknown since the paper didn't include the scan time.

[2]Exact pitch isn't provided; instead it is estimated from Figure 7.

can be found within $5\,\mu\mathrm{m}$ of the surface of the electrodes [21]. It was also noted that the number of fingers doesn't impact the signal to noise ratio significantly because the background noise is "proportional to the area of the electrodes only", but "signal value is proportional to the area of the whole array" and increasing the number of fingers increases both [21].

When measuring EIS, two general approaches are used, specifically looking at the spectrum with or without phase information. A 2012 review of using impedance analysis for microbial electrochemical systems noted that, without phase information, the impedance modulus interpretation is "less sensitive to system parameters", while still providing the important information [17]. Fitting models with higher component counts can lead to overfitting, and masking the underlying effect. The information included in the phase is often not useful when looking at biofilm density [18]. Finally, the systems can be measured using capacitors and resistors only in an idealized EIS circuit model, so the phase information is redundant. For experiments presented in this paper, we used the impedance modulus spectrum.

Chapter 2

Design and Methods

2.1 Overall System Design

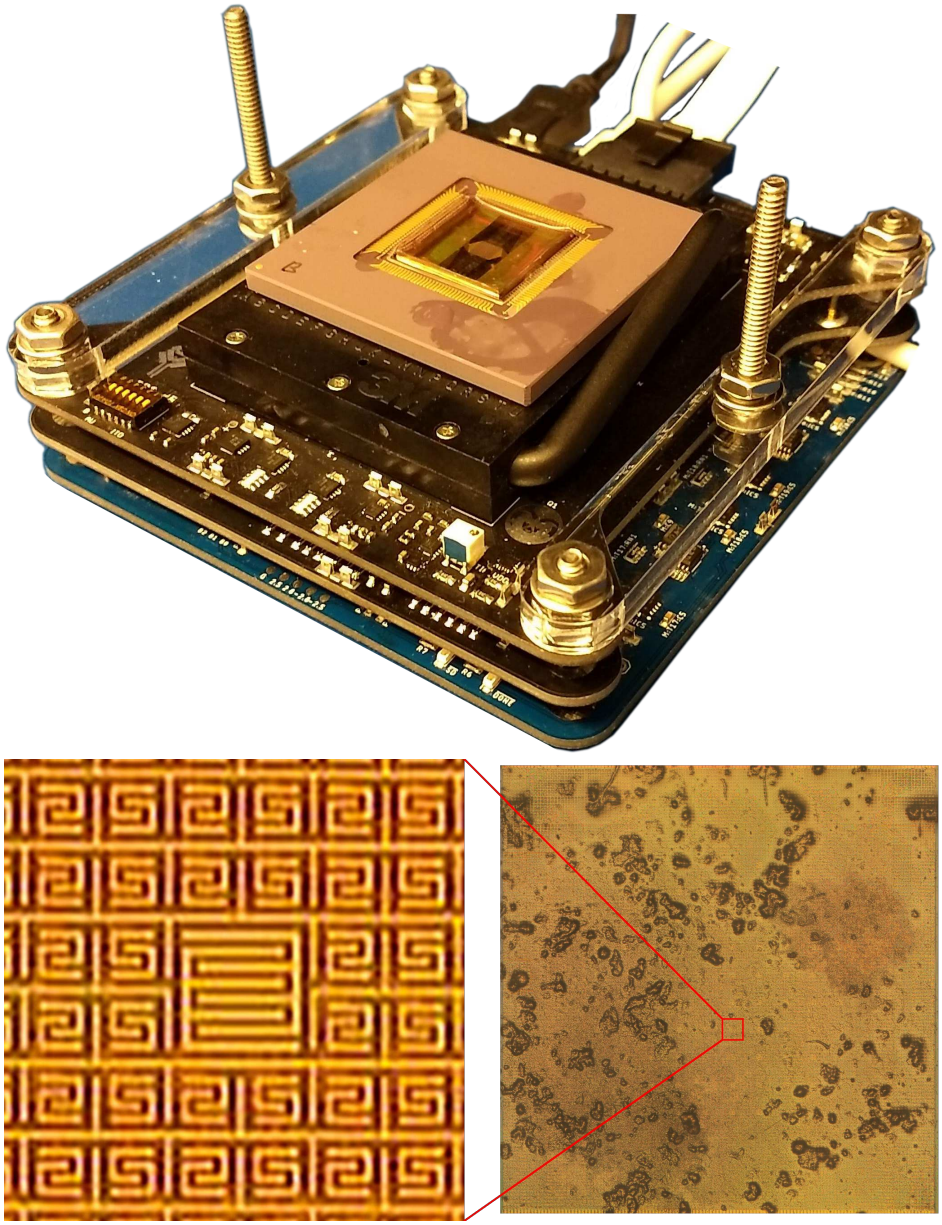

Figure 2.1: CMOS Biosensor Assembled System (top), Closeup of one EIS utility electrode surrounded by other chip electrodes (bottom left), Full $2.2\,\mathrm{mm} \times 2.2\,\mathrm{mm}$ EIS array with *M. Smegmatis* grown on the surface (bottom right)

The 3rd Gen CMOS biosensor platform developed previously at CSU can be used for a variety of electrochemical experiments. The chip, shown in Figure 2.1 has 16k electrodes available for amperometry imaging, and 80 pairs of interdigitated electrodes for impedance spectroscopy. This custom-designed impedance spectroscopy instrument works directly with the CMOS biosensor system to add impedance spectroscopy features to the platform.

As shown in Figure 2.2, the add-on impedance spectroscopy instrument consists primarily of a stimulus generation part, and a readout part, with some level shifting and scaling built in. The stimulus is provided to all the channels which are modeled as a resistance and the outputs are read by dedicated transimpedance amplifiers (TIAs). The outputs from the TIAs are then multiplexed down so they can be read out using a single analog to digital converter (ADC). To operate the $1\,\mathrm{MHz}$, 14-bit resolution ADC needed to sample the signal with the desired speed and quality, the digital SPI-compatible interface operates at a bit rate of $16\,\mathrm{Mbps}$.

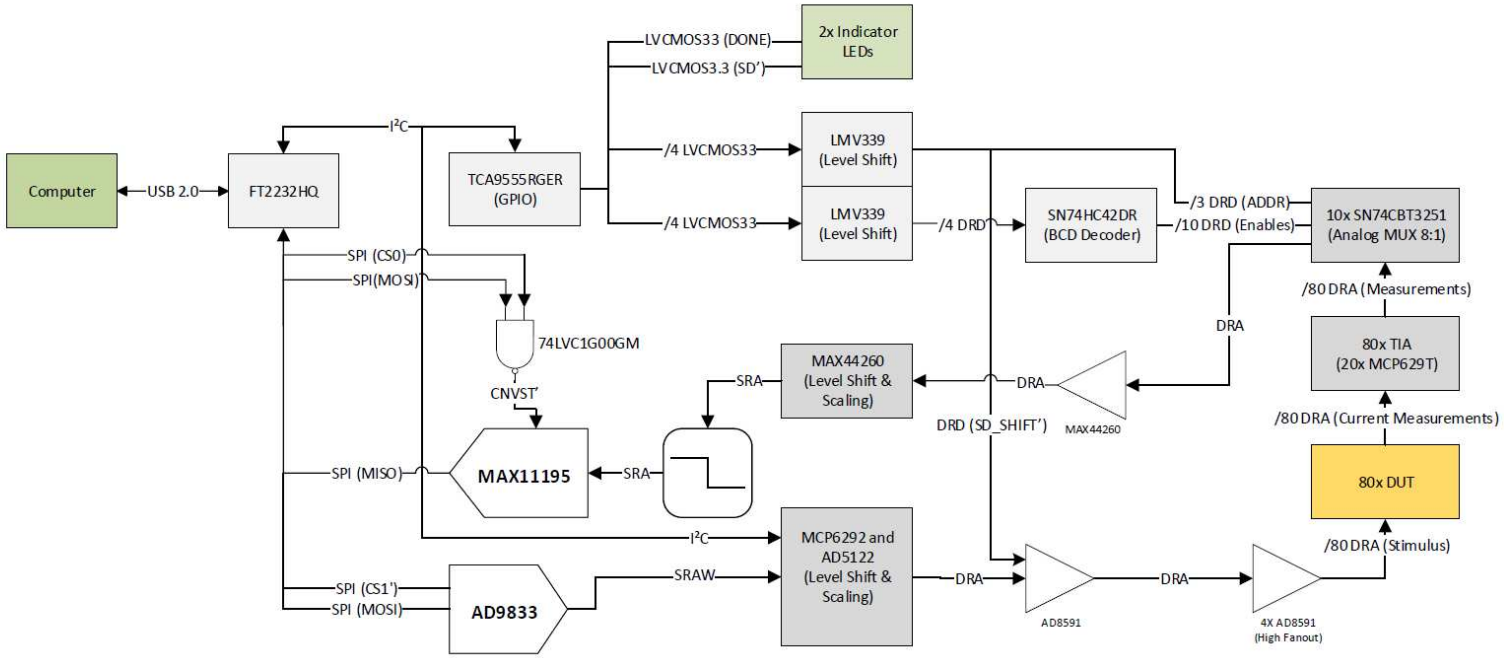

Signal Type Legend:
DRD: Dual Rail Digital (-2.5V to 2.5V)
DRA: Dual Rail Analog (-2.5V to 2.5V, 0V CM)
I²C: Inter-Integrated Circuit Protocol
LVCMOS 3.3: Single Rail 3.3V Digital (0V to 3.3V)
SPI: Serial Peripheral Interface
SRAW: Single Rail Analog Weak (0V to 600mV, 300mV CM)
SRA: Single Rail Analog (0V to 2.5V, 1.25V CM)
USB 2.0: Universal Serial Bus High Speed

Figure 2.2: System Top-Level Diagram

2.2 Electrical System Design

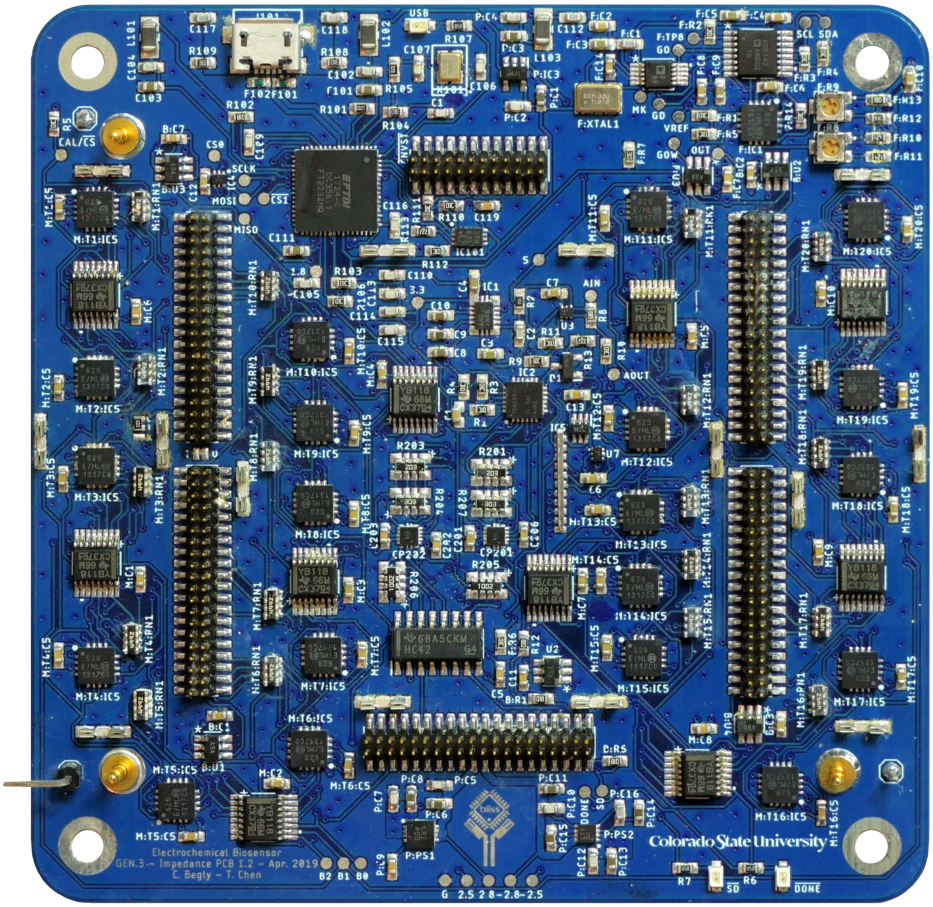

Figure 2.3: Impedance Spectroscopy Board

The impedance spectroscopy instrument consists of the custom instrumentation board shown in Figure 2.3. This board is designed to work as an add-on to the existing Gen 3 CMOS biosensor platform, and it simply plugs into the bottom of the existing device. User control is provided by connecting the device to a computer using the USB port on the side. The following sections discuss the theory, design, and operation of this board.

2.2.1 Function Generation

The stimulus signal for EIS is a single frequency, low amplitude sinusoid, where the frequency can be swept over a large frequency range. For the frequency generation, we use the AD9833 direct digital synthesis (DDS) chip which is capable of generating a fixed amplitude sine wave output from with a maximum frequency resolution[3] of $0.1\,\mathrm{Hz}$. The EIS frequency range of interest varies [10–16, 18–20, 22], but this design focuses on the window from $1\,\mathrm{kHz}$ to $100\,\mathrm{kHz}$ which falls well within the capability of this chip. The chip is controlled directly via the serial-peripheral interface (SPI). The other benefit of this chip is that it is free-running so no CPU time is needed to control stimulus generation.

2.2.2 Stimulus Level-Shifting and Scaling

The output of the DDS chip is a fixed $600\,\mathrm{mV_{pp}}$ sine wave with an offset of $325\,\mathrm{mV}$ from ground. When applying the signal to the electrodes, the signal mean must be at zero to prevent or reduce drift over time. Similarly, the stimulus voltage must be small ($5 - 100\,\mathrm{mV_{pp}}$) so the biofilm isn't damaged [11, 13, 14], and the system operates in the pseudo-linear region of the electrochemical system [17]. This prevents substantial oxidation or reduction products and allows measuring the system impedance magnitude (modulus) at the stimulus frequency.

To take this fixed output signal and tailor it to the desired output amplitude and offset, the signal is passed through an adjustable level shift and scale system. The circuit to do this is shown in Figure 2.4 and uses a dual-channel digital potentiometer (digipot) and four operational amplifiers (op amps). The digital synthesis output is passed into digipot A which scales it down by the factor $\frac{A}{256}$ where A is some value between 0 and 255. The output then buffers and scales this, and subtracts V_{ref}. The resulting output is shown in Equation 2.1.

[3] Using a $25\,\mathrm{MHz}$ master clock

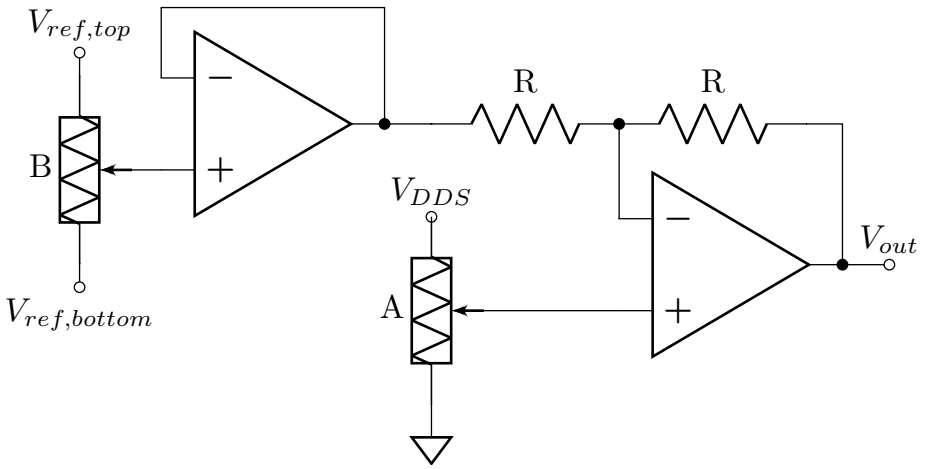

Figure 2.4: Stimulus Level-Shift and Scale Circuit.

$$\begin{aligned} V_{out} &= 2 \cdot \frac{A}{256} \cdot V_{DDS} - V_{ref} \\ &= A \cdot \frac{V_{DDS}}{128} - V_{ref} \end{aligned} \tag{2.1}$$

Digipot B similarly selects a value between its high and low sides, allowing subtraction of any offset in that range. The output is then buffered and used as V_{ref}. The value of V_{ref} can be estimated as shown in Equation 2.2.

$$V_{ref} = B \cdot \left(\frac{V_{ref,high} - V_{ref,low}}{256} \right) + V_{ref,low} \tag{2.2}$$

$V_{ref,high}$ and $V_{ref,low}$ are carefully chosen so that, for $A = B$, the mean of the output signal as measured is zero. To provide this fine adjustment, both $V_{ref,high}$ and $V_{ref,low}$ are generated using the buffered output from a trim potentiometer (trim pot) network as shown in Figure 2.5. Resistors R_1 through R_4 limit the possible adjustment range of the potentiometers to within $\approx 100\,\mathrm{mV}$ of the calculated offset value. Using a potentiometer resistance of $10\,\mathrm{k\Omega}$, $R_1, R_2 = 120\,\mathrm{k\Omega}$,

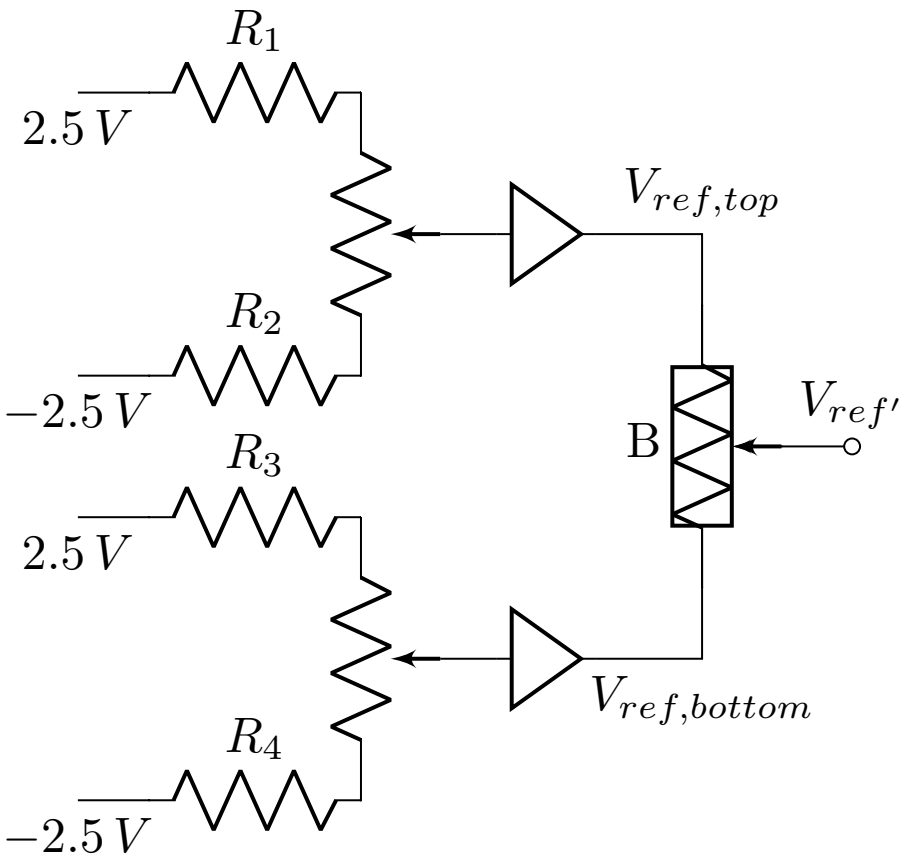

Figure 2.5: Tuning Potentiometer Network

$R_3 = 90.9\,\mathrm{k}\Omega$, and $R_4 = 150\,\mathrm{k}\Omega$, this gives the adjustment ranges shown in Table 2.1. The calibration steps and results are discussed in Section 3.1.

Table 2.1: V_{ref} Low and High Adjustment Ranges

	Min	**Nominal** (mV)	**Max** (mV)
$V_{ref,low}$	-100	0	100
$V_{ref,high}$	489	600	689

2.2.3 TIA

Once the stimulus signal has been prepared, it needs to be applied to each channel, and the sensor output current recorded. This is done using a two-electrode system as shown in Figure 2.6.

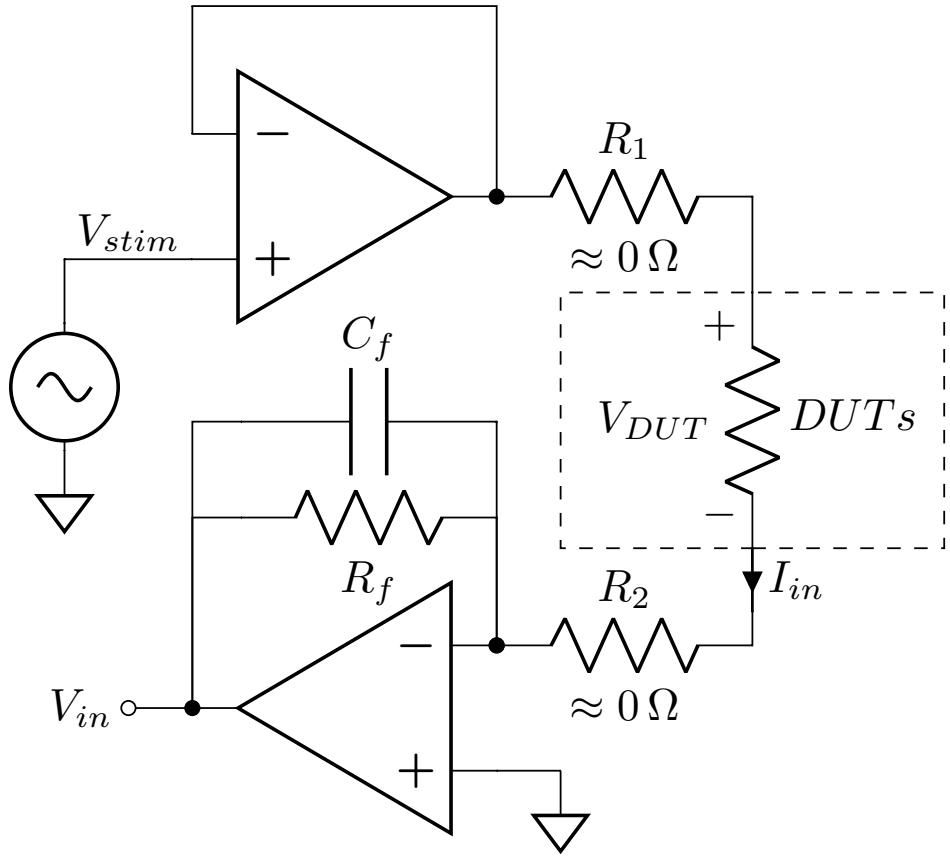

Figure 2.6: Channel Stimulus and TIA Readout

The stimulus voltage is fanned out to four buffers (one for each quadrant of the device) and then these are connected to one side of the electrodes. R1 and R2 represent the non-ideal resistances in the connection to the electrodes, and are low in value. The stimulus across the electrodes is slightly less than V_{stim} as shown in Equation 2.3, and the error percentage is shown in Equation 2.4.

These equations show that as long as $R_{dut} \gg R_1 + R_2$ the error is small and tends towards zero[4].

$$V_{dut} = V_{stim} \cdot \frac{R_{dut}}{R_{dut} + R_1 + R_2} \tag{2.3}$$

$$\%\,\text{error} = \frac{R_1 + R_2}{R_{dut} + R_1 + R_2} \cdot 100 \tag{2.4}$$

The transimpedance amplifier (TIA) in the readout part of each channel holds the working electrode at a virtual ground (or near it, subject to R2) and converts the current to an output voltage as shown in Equation 2.5. Once V_{in} is known, the resistance across the electrodes is computed as shown in Equation 2.6. As expected, as long as $R_1 + R_2$ is small, the error is small.

$$V_{in} = -I_{in} \cdot R_f \tag{2.5}$$

$$R_{dut} = -\frac{V_{stim}}{V_{in}} \cdot R_f - R_1 - R_2 \tag{2.6}$$

The feedback capacitor C_f helps with stability and noise reduction by acting in conjunction with R_f as a low-pass filter with a corner frequency of $\frac{1}{2\pi R_f C_f}$. A lower corner frequency means less noise is passed through, and blocks interference, but there is some attenuation close to the corner frequency. This tradeoff is discussed more in Section 2.2.6.

2.2.4 MUX

Each of the eighty channels has a dedicated TIA, and then the outputs are multiplexed down to a single shared analog-to-digital converter (ADC). As shown

[4]DUT stands for device-under-test and represents the electrodes and whatever is between them

in Figure 2.7, ten 8:1 muxes (TS5N118DBQR) are used to take blocks of 8 channels down to 10 block signals. The outputs of these are then shorted together, and the enables on the muxes are chosen so only one is enabled at a time. The muxes are rail-to-rail analog muxes with a bandwidth of $25\,\mathrm{MHz}$.

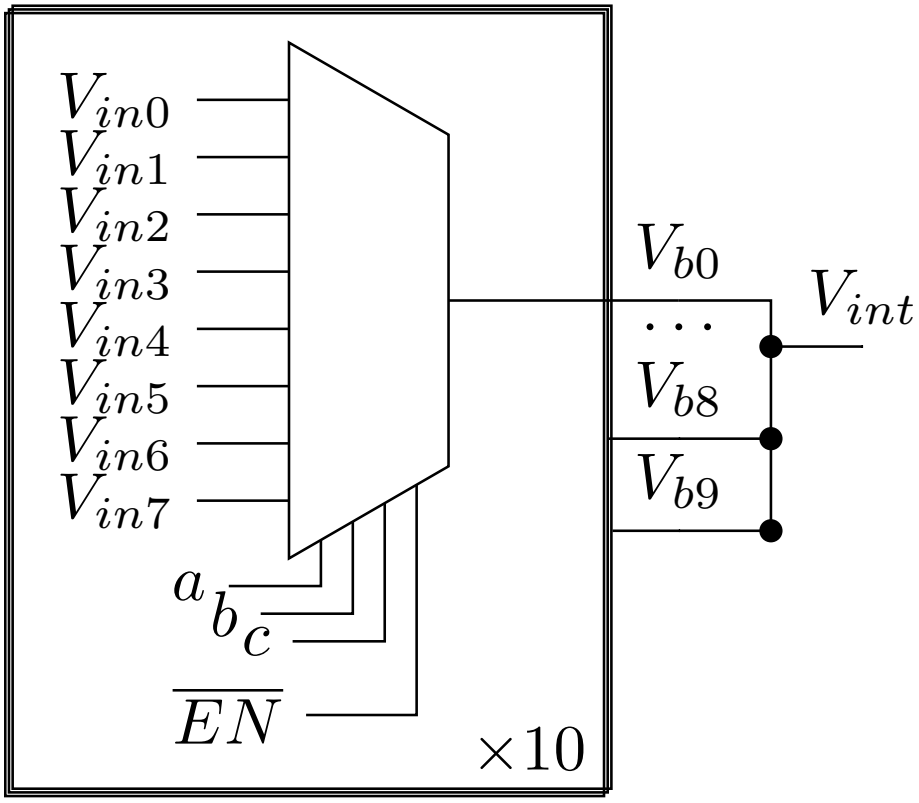

Figure 2.7: 80:1 Multiplexing

There is also a 2:1 MUX that chooses between V_{int} and V_{ext} before the Level-Shifting and Scaling stage to allow this system to sample external voltage signals. It allows integrated sampling of the existing system, and is used during the automated system calibration.

2.2.5 Input Level-Shifting and Scaling

The input to the system needs to be scaled from the $\pm 2.5\,\mathrm{V}$ dual-rail side to the $0 - 2.5\,\mathrm{V}$ range of the ADC. This involves scaling it down by a factor of 2 and

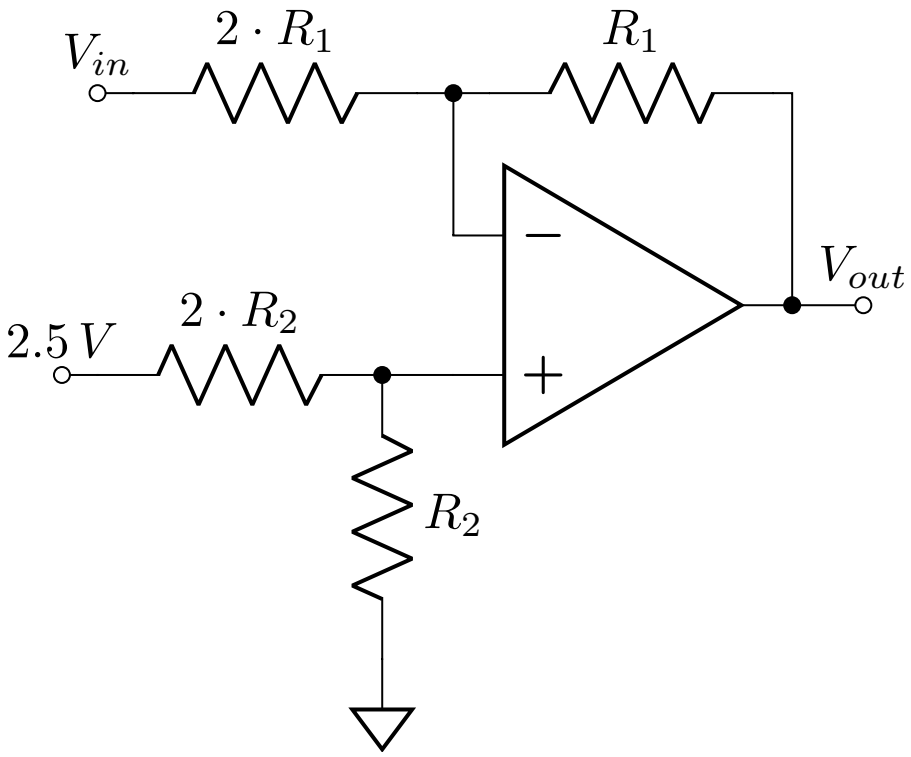

Figure 2.8: Input Level-Shift and Scale

shifting it up by $1.25\,\mathrm{V}$. This can be done using an inverting amplifier with a non-zero reference as shown in Figure 2.8. This circuit gives the desired V_{out} as shown in Equation 2.7

$$V_{out} = -\frac{1}{2}V_{in} + 1.25 \tag{2.7}$$

2.2.6 ADC

To sample the signals, the ADC must be capable of sampling more than twice as fast as the highest frequency component in the signal. The ADC used is the MAX11195 14-bit ADC capable of up to $2\,\mathrm{MSPS}$ which has a SPI-compatible interface. Since the highest desired signal frequency in our system is $100\,\mathrm{kHz}$, the Nyquist frequency is $200\,\mathrm{kHz}$ and sampling will have to be faster than that to

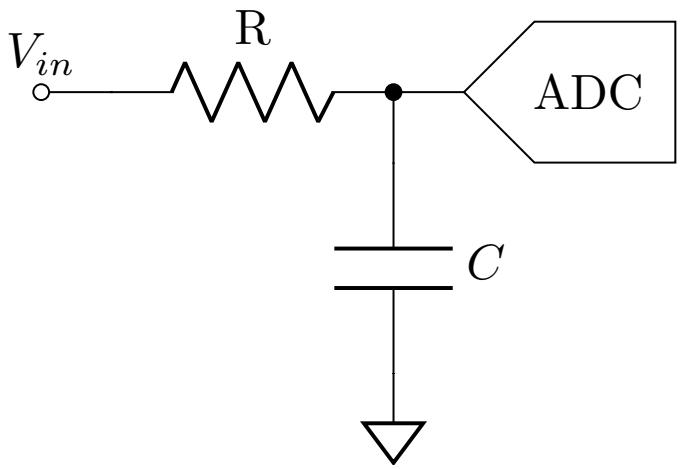

Figure 2.9: ADC and Anti-Aliasing Filter

avoid aliasing. An RC anti-aliasing filter is placed in front of the ADC to attenuate higher frequency noise. In practice, a perfect anti-aliasing filter is not possible (and a single-pole RC filter isn't close), so by oversampling by 10x, we allow for a $400\,\mathrm{kHz}$ transition band $\left(\frac{1\,\mathrm{MHz}}{2} - 100\,\mathrm{kHz} = 400\,\mathrm{kHz}\right)$. The frequency dependent gain is shown in Equation 2.8.

$$|A| = \sqrt{\frac{1}{1 + (2\pi f RC)^2}} \tag{2.8}$$

From this we can choose the anti-aliasing filter by how close we can get to our maximum frequency without introducing too much gain error. For example, with $R = 7.5\,\Omega$ and maximum allowed gain error of 1% at $100\,\mathrm{kHz}$, C must be less than $30.24\,\mathrm{nF}$ ($f_c \geq 702\,\mathrm{kHz}$). Using the manufacturer recommended $1\,\mathrm{nF}$ capacitor, drops the error to $< 0.001\,\%$ but increases the amount of noise that is let through.

2.2.7 USB Interface and Digital Control

All control logic is handled by an FT2232H chip from FTDI which provides two Multi-Protocol Synchronous Serial Engine (MPSSE) channels over USB. One

channel is configured to SPI serial, while the other is configured as I^2C. All addressing and enable bits are handles by an I^2C controlled general purpose IO (GPIO) extender as shown in Figure 2.10.

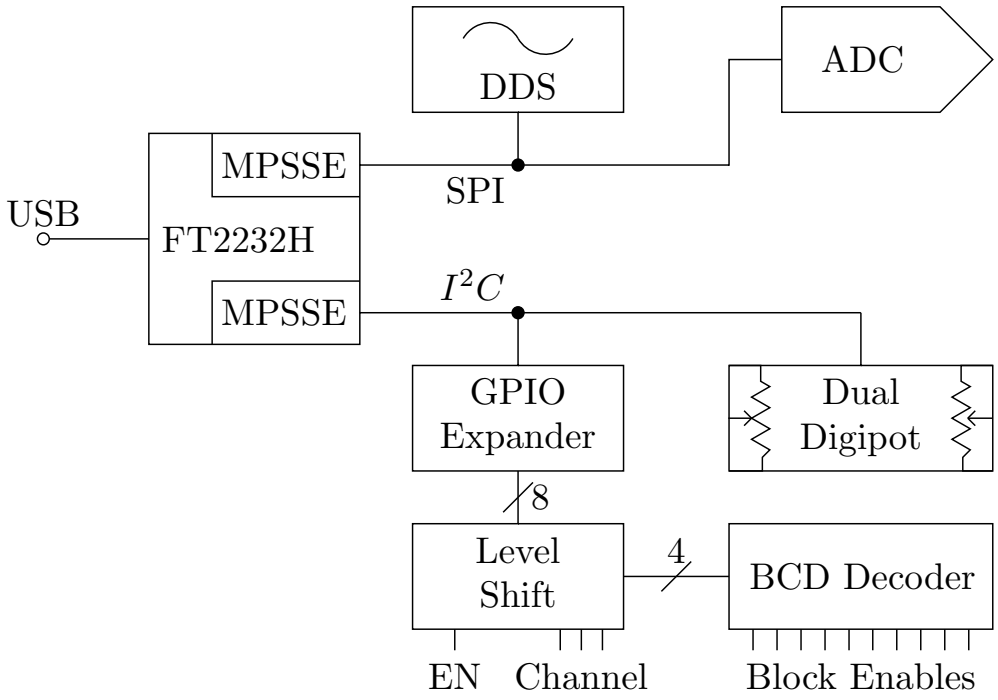

Figure 2.10: Digital Control Top-Level Diagram

Three bits are used to select 1-of-8 on the muxes, and then 4 bits are passed through a binary coded decimal (BCD) converter to enable one of the 10 muxes at a time. This chip has a break-before-make design to ensure that only one MUX is ever enabled at a time. A system enable bit is tied to the stimulus output, and defaults to OFF. This allows the software to fully configure the desired waveform before applying it to the system to avoid any undesired glitches or unknown states.

2.3 Software Design

2.3.1 Overview

The software for the device is written in C++, and consists of a base library overlaying the FTD2XX library, and a graphical user interface (GUI) written in Microsoft Foundation Classes (MFC) for easy user interaction. This logical arrangement was chosen to allow easier integration of the device into other applications or scripts as needed, so making things like a Matlab library or Python library would be easy.

The base library consists of a custom layer over the core FTD2XX library because the manufacturer provided library was too slow. For I^2C in the system, the slowdown was not a problem. However, driving the high-speed SPI line for the ADC was due to baked in timing concerns. Using the manufacturer provided LibMPSSE-SPI, the fastest possible sampling speed measured was approximately $340\,\mathrm{SPS}$, limited mostly by that library's handling of the chip-select lines. Using the custom library, the maximum sampling speed[5] was increased to $937.5\,\mathrm{kSPS}$.

The library also includes objects that allow direct control over all chips connected to the FTDI chip, including the function generator, digipot, ADC, and GPIO chips. These integrate directly into the custom FTDI library and allows any software that develops on top of the board complete control over the system. Separate documentation is provided for this library as a whole, and the documentation details both the expected uses and alternative uses.

2.3.2 User Interface

The User Interface is shown in Figure 2.11. The user can connect to any connected device, adjust the stimulus settings, and take impedance readings, spectrum readings, or raw readings. There are also tools for looking at the ef-

[5]Assumes $12\,\mathrm{MHz}$ master clock for the FT2232H chip

fect of stimulus voltage on the result, and for displaying a live (updated every 2 seconds) view of the heatmap. The user can click on any location on the image to get the exact value, and the data is also available in CSV format for further processing in Matlab, R, or Python.

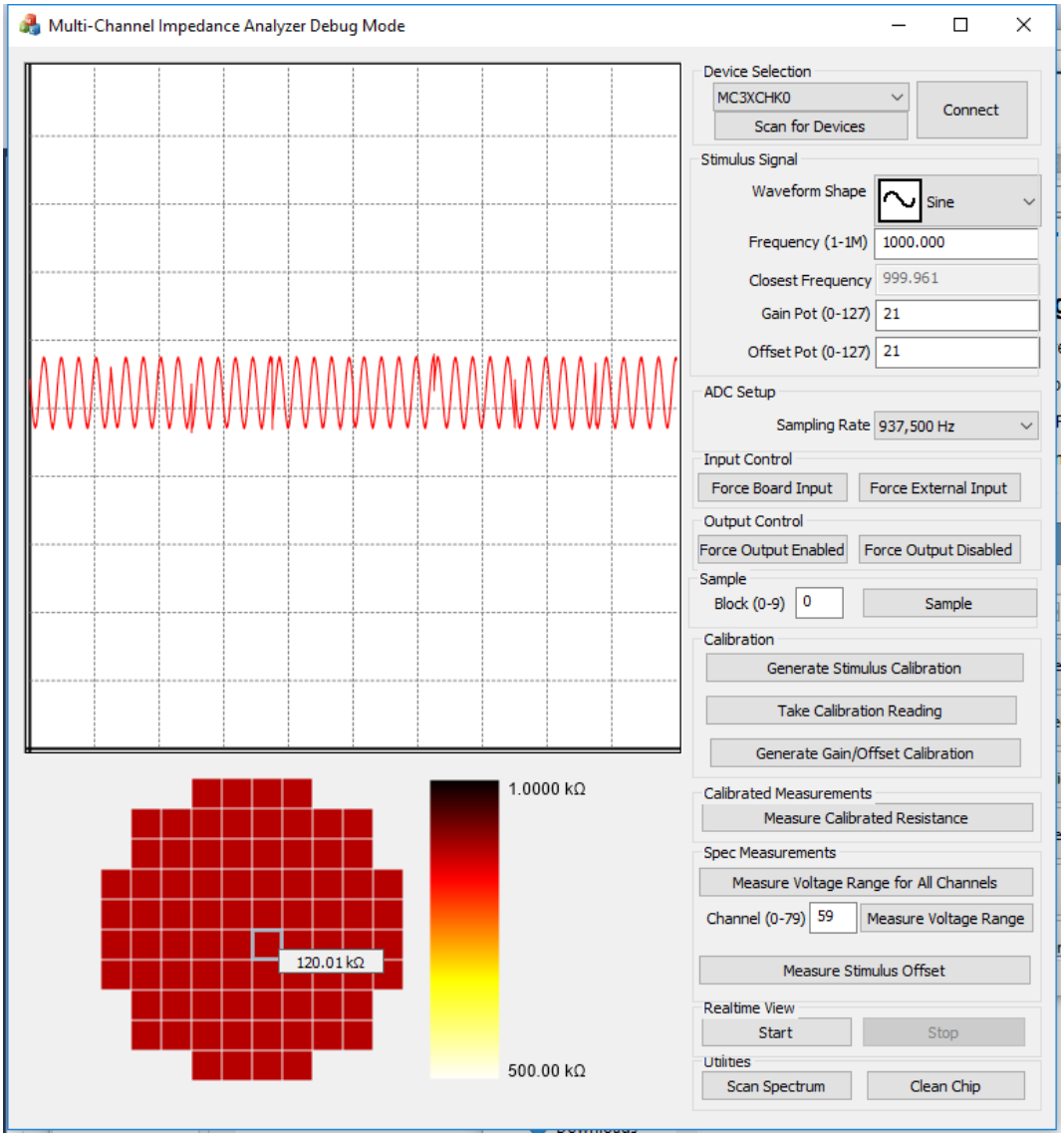

Figure 2.11: Debug User Interface

Table 2.2: Comparison of Frequency Measurement Algorithms

Algorithm	Pros	Cons
FFT	Fast	Too inaccurate for LLS
STZX	Fast	Noise intolerant
DTZX	Good noise tolerance	Noise amplitude must be estimated
STZX+	Fast, good noise tolerance	Frequency must be known

2.3.3 Measurement Algorithms

Since the system functions by applying a sine wave to the system and then measuring the output sine wave to see how much the amplitude changed, accurate measurement of amplitude is important. A simple max/min difference algorithm is not ideal because noise in the system will typically make this an overestimate of peak-to-peak voltage, particularly at low amplitudes. The other issue is that it doesn't provide an estimate of how close to sinusoidal the output is which can be important for ruling out bad measurements or substantial interference. Instead, we use a linear least squares (LLS) fit. While this is computationally more intensive, it provides a high quality measurement, even at low SNR, provided the noise is normally distributed.

Frequency Measurement

To get a linear least squares fit, we first need to estimate the frequency of the measured sinusoid. There are several algorithms for this including fast Fourier transform (FFT), single-threshold zero-crossing detection (STZX), dual-threshold zero-crossing detection (DTZX), and single threshold zero-crossing detection with known frequency (STZX+). The comparison between these algorithms is shown in Table 2.2.

Fast Fourier transform estimates are not useful for measuring the frequency to the exactness needed for LLS because the frequency resolution is limited to bin widths as shown in Equation 2.9.

$$\Delta_f = \frac{F_s}{N}, \tag{2.9}$$

In our case ($F_s = 1\,\mathrm{MHz}, N = 1000$) the frequency resolution is $1\,\mathrm{kHz}$ which is too broad to be used. While spectrum interpolation can give a closer idea of where the frequency is, and increasing the number of points in the FFT can also help, these increase both the computational complexity and sampling time, while still giving results that are at best comparable to other techniques.

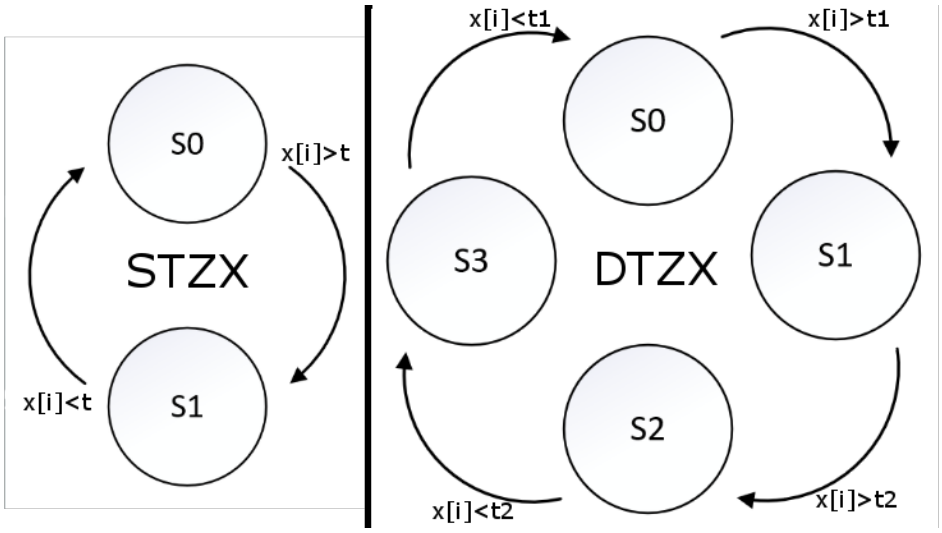

Figure 2.12: STZX and DTZX State Machines

STZX is useful when looking at signals that are monotonically increasing on rising edges and monotonically decreasing on falling edges. This typically limits its use to signals which have little noise, or smoothed signals. It operates by a simple state machine as shown in Figure 2.12 that looks for rising and falling

edges crossing some threshold in the middle of the signal, counting up the whole number of crossings (rising and falling pair), and then dividing the distance from the first crossing to the last crossing by the number of whole crossings to get the period of the signal. However, it fails when the noise causes the algorithm to detect many zero-crossings on the same edge. DTZX solves this problem by requiring the signal to cross two thresholds before registering a crossing. As long as the two thresholds are further apart than the expected maximum noise contribution, this algorithm is noise tolerant. This difference is shown in Figure 2.13.

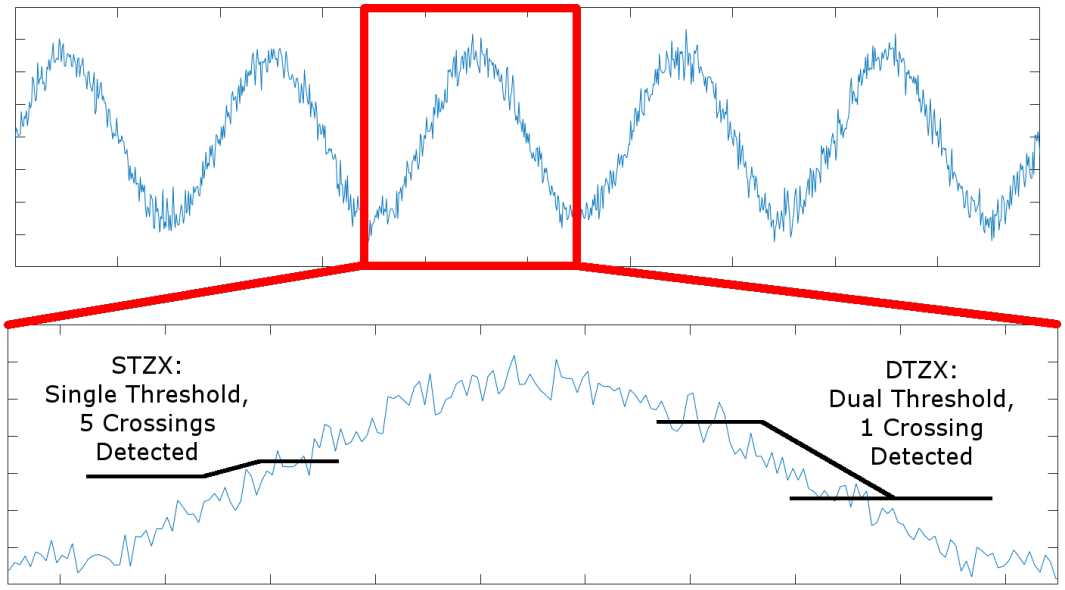

Figure 2.13: STZX vs. DTZX Comparison

STZX+ is similar to STZX, but to deal with the possibility of multiple false crossings near a true crossing due to noise, STZX+ advances the algorithm by some minimum number of samples (jump distance) once a crossing is detected. Using a fixed jump distance like 10-20 samples can work OK for high frequency signals, but still fails on lower frequency signals because the slope is so shallow that the jump will not get far enough away. The optimal jump distance is 1/4 of

a period of the signal because that goes from the crossing to either the next peak or valley which is maximally away from the threshold. This is why for STZX+ it is best to have an estimate of the frequency. Since this system applys the stimulus frequency, and the measured frequency will be close, STZX+ tends to perform best with a balance between performance and speed.

The accuracy varies with SNR as shown by Figure 2.14. This graph was generated by simulating ten thousand noisy signals at each decibel step, and testing them on all three algorithms to see which algorithm detected the frequency correctly. As it shows, both STZX+ and DTZX perform better than STZX. STZX+ performs better than DTZX at low SNRs which makes it useful for extending the upper range of the possible resistances that can be measured.

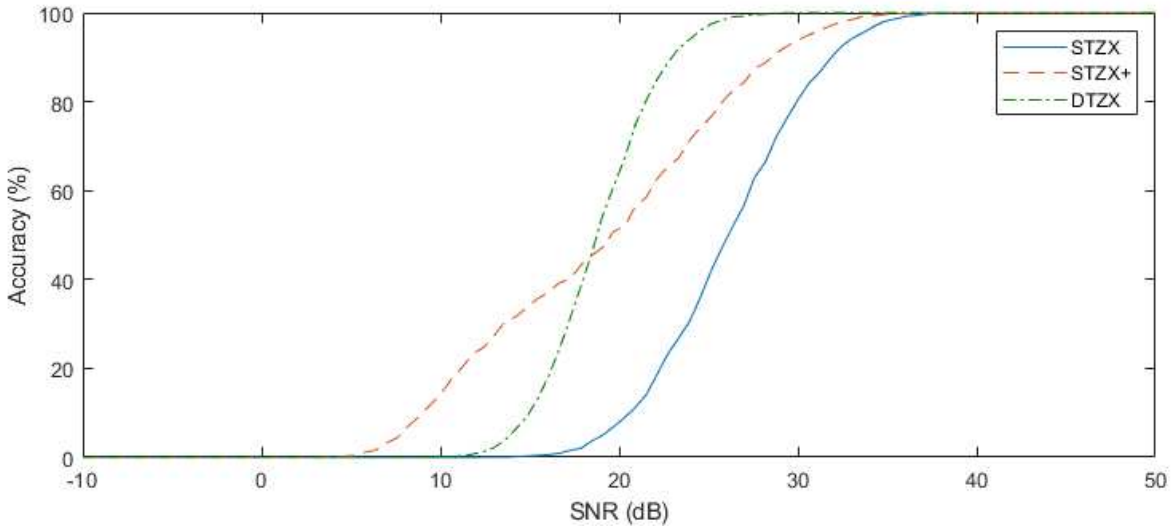

Figure 2.14: Zero-Crossing Algorithms Comparison

Amplitude Measurement

Once there is an accurate frequency estimate, it can be used to build the basis vectors for the linear least squares (LLS) fit. Fitting a sinusoidal function with some offset can be done using cosine and sine vectors with the same frequency,

and a constant vector. The resulting features matrix is shown in Equation 2.10 where n is the number of data points in the sampled signal, and N is the measured period of the signal.

$$\mathbf{X} = \begin{pmatrix} 1 & cos(2\pi(0)/N) & sin(2\pi(0)/N) \\ 1 & cos(2\pi(1)/N) & sin(2\pi(1)/N) \\ 1 & cos(2\pi(2)/N) & sin(2\pi(2)/N) \\ \vdots & \vdots & \vdots \\ 1 & cos(2\pi n/N) & cos(2\pi n/N) \end{pmatrix} \tag{2.10}$$

Using this feature matrix, we can compute a transformation matrix M by minimizing the residual sum of squares. Full derivation of this technique is discussed in Appendix D. The result is shown in Equation 2.11.

$$\mathbf{M} = (\mathbf{X}\mathbf{X}^T)^{-1}\mathbf{X} \tag{2.11}$$

This can then be cached as needed, and used to compute the weights vector using a single matrix multiplication with the sample vector $\vec{y}$ as shown in Equation 2.12.

$$\beta = \mathbf{M}\vec{y} \tag{2.12}$$

$$R^2 = 1 - \frac{SS_{residual}}{SS_{total}} \tag{2.13}$$

Using β, the estimate for y ($\hat{y}$) can be calculated as shown in Equation 2.14, and used to compute the coefficient of determination (COD) to provide a rough

measure of how well the model fits the data. The coefficient of determination is computed as shown in equation 2.13.

$$\hat{y} = \beta_0 + \beta_1 cos(...) + \beta_2 sin(...) \tag{2.14}$$

Since the model consists of the sum of a cosine and sine of the same frequency, we can compute the amplitude of the sinusoid formed by their weighed sum as shown in Equation 2.15.

$$A_{meas} = \sqrt{\beta_1^2 + \beta_2^2} \tag{2.15}$$

The final resistance can then be computed using the gain and offset correction factors as discussed in the calibration section, and using the modified version of Equation 2.6 shown below.

$$R_{dut} = \frac{A_{stim}}{A_{meas}} \cdot G_{nom} \cdot G_{cf} - O_{cf} \tag{2.16}$$

2.4 Design Validation

2.4.1 Real-Time Flow Validation

For real-time flow validation, a simple test was designed using a microfluidic system. A flow joiner was set up to join three streams. The outer two streams flowed deionized (DI) water (high resistance) at a rate of $90\,\mu\mathrm{L/hr}$ while the middle stream was set up to release phosphate buffered saline (PBS) (low resistance) at a rate of $10\,\mu\mathrm{L/hr}$. When combined, the system allows the PBS to form a

small stream in the middle third of the chip array, while the DI water on the outer edges remains highly resistive. Spectrum measurements were taken to determine a frequency with good separation. Then samples were taken at that frequency once every 2 seconds in real-time display mode. The DI water was pumping the whole time, while the PBS was turned on and off to show the live results. As discussed in Section 3.2.4, DI water had a resistance greater than $680\,\mathrm{k}\Omega$ while the PBS had a resistance of close to $13\,\mathrm{k}\Omega$.

2.4.2 Biofilm Validation

The design validation also was performed by growing a biofilm on the surface of the chip and then looking at the relationship between the resistance measured and the optical coverage of the electrodes. The chip was initially sterilized at $121\,^{\circ}\mathrm{C}$ by autoclave. The surface was prepared for bacterial attachment by crosslinking small sheared fragments of DNA (Sigma) at $10\,\mu\mathrm{g/mL}$ in 1:1 ratio of water to DNA Binding Buffer (Thermo Fisher). Surface of the chip was incubated at room temperature for 2 hours, and then rinsed with water and dried. Finally, the chip was UV irradiated to crosslink DNA and sterilize growth surface.

Mycobacterium smegmatis was grown in standard 7H9 broth supplemented with 10% OADC and 0.05% Tween-80. Bacteria was grown to an optical density at $600\,\mathrm{nm}$ (OD600) of 1.0. Bacteria were washed with RPMI 1640 with 10% FBS and diluted to an OD600 of 0.1. $500\mu\mathrm{l}$ of bacteria solution was added to the surface of the chip, centered on the electrode array. The chip was then incubated at $37\,^{\circ}\mathrm{C}/5\%\,\mathrm{CO_2}$ for 24 hours. Media was then replaced with fresh media, and incubated for another 24 hours. In the latest experiment, media was replaced and incubated for another 24 hours to allow for more bacterial growth.

Prior to electrical or optical imaging, the media of the chip was flushed five times using $0.5\,\mathrm{mL}$ of fresh media each time, to remove any free-floating bacteria.

Flushing was done by tipping the chip slightly and carefully removing the old media on one side then replacing with new media on the other. Clean media was then added to the chip as needed to keep it from running low or drying out, and to ensure that the whole electrode area was covered during measurements.

The chip was then placed on the instrument platform, and a spectrum scan was completed, scanning from $10\,\mathrm{kHz}$ to $100\,\mathrm{kHz}$ with a stimulus of $100\,\mathrm{mV_{pp}}$ on all channels. The results were saved for further analysis. The chip was then removed and prepared for fluorescent imaging.

Biofilm coverage was visualized with LIVE/DEAD BacLight Bacterial Viability Kit (Fisher) as per manufacturer instructions. Live bacteria were stained with SYTO 9 and dead cells or extracellular DNA was stained with propidium iodide.

The imaging was performed using an Olympus BX61W scope with a Hamamatsu Orca2 camera and an Olympus UPlanFLN 4x / 0.13 objective. The initial photos were taken using Metamorph imaging software, and then the photos were stitched together using Photomerge™ Panorama software in planar mode to provide an image of the whole surface of the chip at once.

Chapter 3

Results and Discussion

3.1 Calibration

Each device has is slightly different due to process variations in the components. To deal with this, there are three separate calibration steps that need to be run on each device prior to using to get the most accurate results. These can be performed prior to shipping the device to the end user, and the calibration data can be loaded by the software on installation.

3.1.1 Zero-Mean Calibration

The stimulus circuit discussed in Section 2.2.2 has two trim potentiometers (trimpots) designed to allow tuning the circuit so the stimulus DC level is as close to zero as possible. Prior to other calibration of the device, the stimulus must be zero-mean calibrated.

1. Connect a four channel oscilloscope to all four quadrant stimulus outputs
2. Set gain and offset digipots both to 0
3. Adjust the $V_{ref,low}$ trim pot until the signal average is as close to 0 as possible
4. Set gain and offset digipots both to 255
5. Adjust the $V_{ref,high}$ trim pot until the signal average is as close to 0 as possible

The results of calibration on one of the devices is shown in Table 3.1. By using this calibration method, over the full range of stimulus signals, the offset doesn't vary by more than $3\,\mathrm{mV}$.

3.1.2 Stimulus Voltage Calibration

Calibration of the stimulus voltage is important to get accurate resistance measurements. Generating the calibration is simple through the user interface. The user can click the *Generate Stimulus Calibration* button, and follow the prompts. It walks the user through connecting each quadrant to the external sensing input, and then the voltages are measured for all gain settings. The calibrated stimulus values are within 0.2% of the values manually measured using an external scope during validation. The details are summarized in Table 3.1.

3.1.3 Gain/Offset Calibration

Each channel has a slightly different gain error due to feedback resistor variation. There is also a small variation in the series resistance due to varying trace lengths. To compensate for this, and calibrate all the resistance measurements for the device, this requires measurement of a known resistance. The known resistances for all channels are provided by three calibration boards of different values including the one shown in Figure 3.1.

Each resistance on the board is manually measured using a GwInstek LCR-821 LCR meter to get the known resistance measurement. Each board provides a single data point for each channel which can then be fit to compute a gain correction factor (G_{cf}) and an offset correction factor (O_{cf}). Once a calibration board is created, it can be used to calibrate multiple devices, nearly automatically.

To calibrate each new device, a Calibration board with known resistances for all channels is connected, and then calibration readings are taken through the user interface by clicking *Take Calibration Reading*. Once three or more calibration readings have been taken, clicking *Generate Gain/Offset Calibration* in the user interface and following the prompts generates the final gain and offset

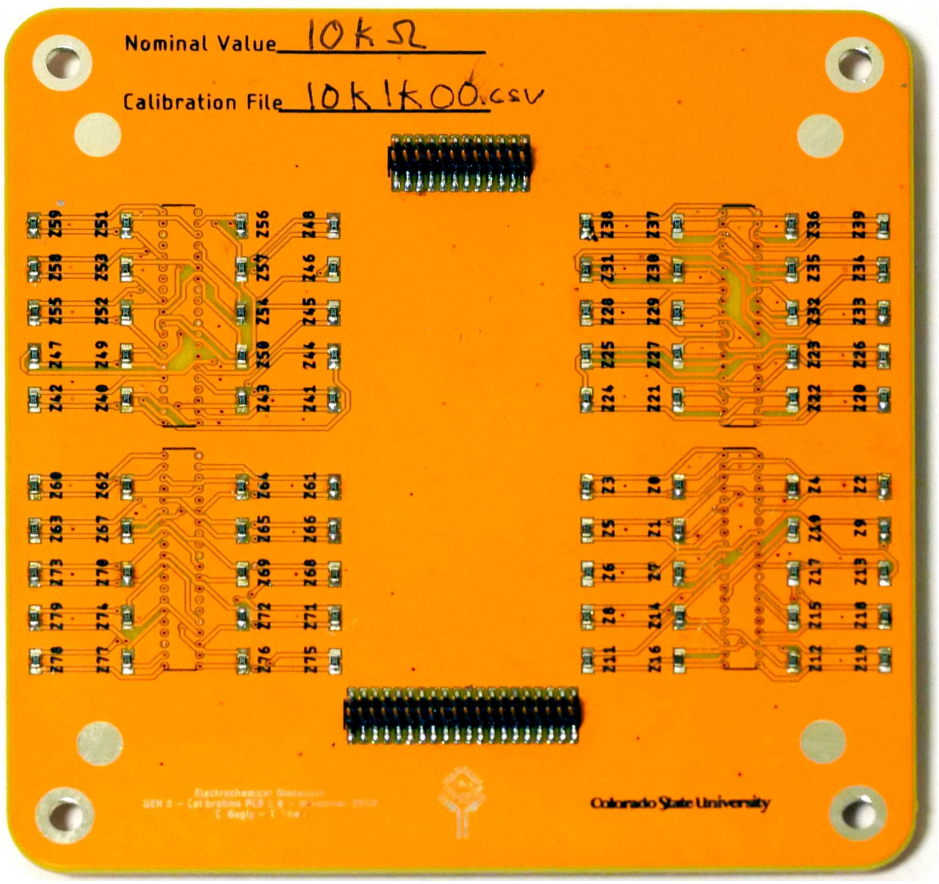

Figure 3.1: Calibration Board

compensation values for the device. Following calibration, the impedance error is less than 0.7%. The rest of the details are summarized in Table 3.1.

3.2 Device Validation

3.2.1 Noise Performance

The analog front-end noise needs to be low so measurements can be taken over a wider range of resistances. Measurement of the noise performance of the front-end was performed using a Keysight MSOS254A scope to measure the noise spectrum at the input to the ADC when there is no input to a given channel. The spectrum is shown in Figure 3.2.

All noise figures are summarized in Table 3.1.

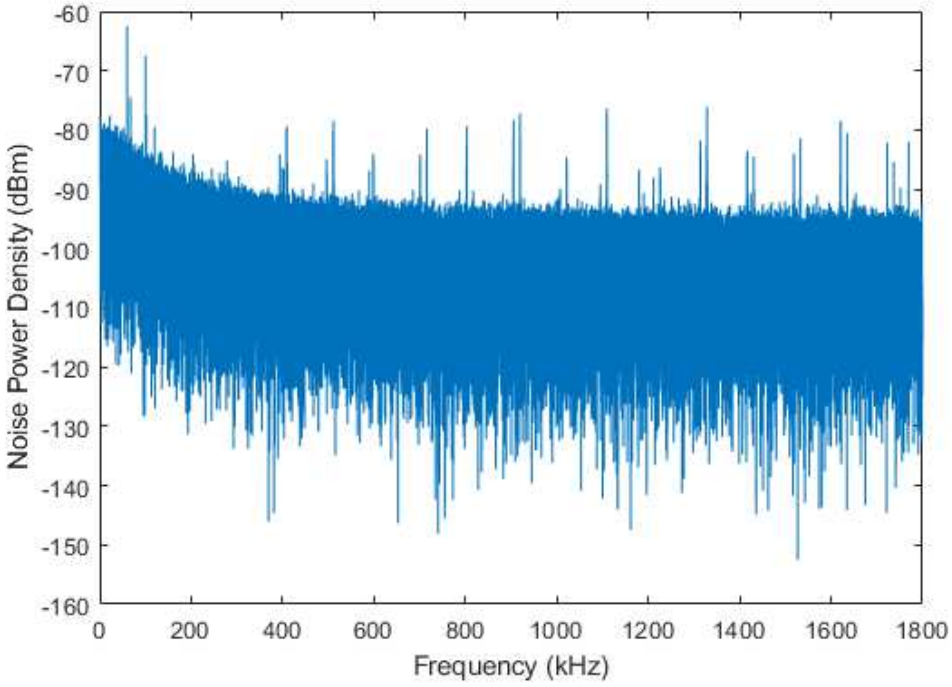

Figure 3.2: Noise Spectrum

3.2.2 Impedance Modulus and Stimulus Range

Impedance modulus accuracy is measured by applying known resistance values to all channels following calibration, and measuring the error between the known value and the measured value over several points in the expected Impedance space. The known values are measured using a GwInstek LCR-821 LCR meter, which has an accuracy of 0.05% and 5 significant figures.

Over most of the impedance range, the error is near 0.5%, but it drops at the high end due to poor SNR, and on the low end due to the limitations in front-side voltage swing. For example, with a stimulus of $100\,mV_{pp}$, the accuracy is best over the range $10\,\mathrm{k}\Omega$ - $120\,\mathrm{k}\Omega$ but drops for values over $500\,\mathrm{k}\Omega$ and under $1\,\mathrm{k}\Omega$. The possible operating region that maintains a resistance error of less than 1% is shown in Figure 3.3. As long as the user keeps the values within these ranges, the resistance values are within the valid calibrated range. Operating slightly outside of this will still give readings, but error may increase slightly. Operating

too far outside the range will cause the measurement fit COD to drop below the internal threshold and the device will not give a value and instead will warn the user that the reading is “Out of range”. When readings are taken, the user can look at the COD for a given measurement to see the goodness of fit. Summary of the measurement accuracy is included in Table 3.1.

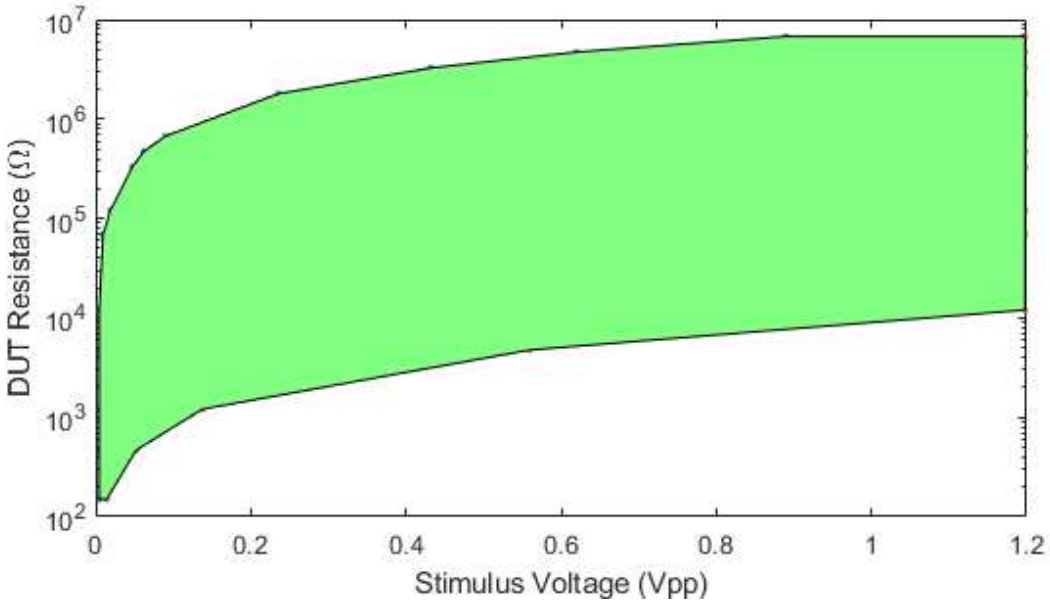

Figure 3.3: Operating Region with Error <1%

3.2.3 Summary of Device Specifications

Table 3.1: Device Measured Specifications

Specification	**Value**	**Unit**
Sampling		
Measurement Time per Channel, per Frequency*	1.23	ms
Impedance		
Range @100 $\mathrm{mV_{pp}}$**	1-680	$\mathrm{k\Omega}$
Max Error ($10 - 120\,\mathrm{k\Omega}$)	0.698	%
Max Error ($1 - 10\,\mathrm{k\Omega}$)	1.6521	%
Stimulus		
Stimulus Voltage Range	4.68-1193	$\mathrm{mV_{pp}}$
Stimulus Voltage Resolution	4.68	$\mathrm{mV_{pp}}$
Max V_{pp} Error	0.198	%
Max Offset Error†	12.6	mV
Max Single Quad Offset Error†	3.0	mV
Frequency Range	1-100	kHz
Frequency Resolution	0.093	Hz
Noise		
Total Noise Power	0.03742	$\mu\mathrm{V}^2$
Avg. Spectral Density	144.22	$\mathrm{nV}/\sqrt{\mathrm{Hz}}$
Spot Noise @ $1\,\mathrm{kHz}$	814.77	$\mathrm{nV}/\sqrt{\mathrm{Hz}}$
Spot Noise @ $10\,\mathrm{kHz}$	575.05	$\mathrm{nV}/\sqrt{\mathrm{Hz}}$
Spot Noise @ $500\,\mathrm{kHz}$	102.90	$\mathrm{nV}/\sqrt{\mathrm{Hz}}$
Read Channel		
Bandwidth	159	kHz
Attenuation @ $100\,\mathrm{kHz}$	-1.4	dB
Phase Margin	60.	$^\circ$
Swing	$\pm$2.327	V
Power Consumption		
Add-On Only‡	300	mW
Full System‡	1.024	W

* Assuming high confidence mode, worst case USB timing, and 8192 samples/channel

** For full range specifications, see Figure 3.3.

† 3σ estimate of maximum

‡ Estimated maximum power under full load

3.2.4 Wet Validation Results

Flow Validation

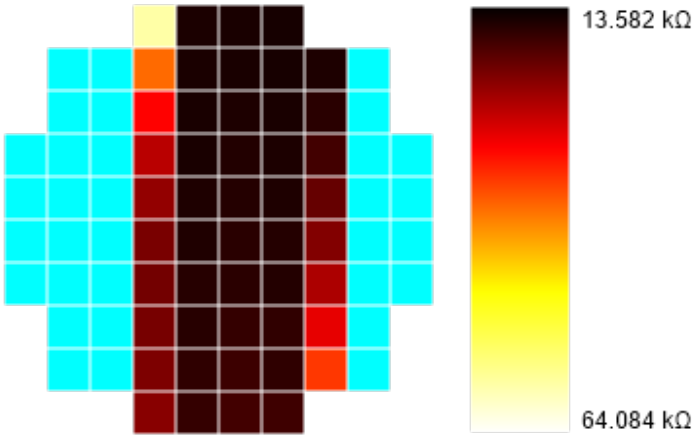

Figure 3.4: Flow Image Taken While PBS is Pumping

The flow test showed that the device could be used to illustrate the conductivity of the solution change in real-time. It also showed that the microfluidic technique produced a small conductive stream down only a small portion of the chip as shown in Figure 3.4. The teal areas in the image represent high resistance areas. The PBS flow enters on the top middle as evidenced by the lower resistance in the image. As it continues across the array towards the bottom, the PBS solutes diffuse into the DI water, lowering the conductivity of those areas.

Biofilm Validation

The resulting fluorescent image from the biofilm growth experiment is shown in Figure 3.5. The dashed line boxes show where the electrodes are located on the surface. The surface reflects a fair amount of the emitted green light, so there is a bit of background bleed, but areas with higher coverage still have higher intensities. For the purposes of this experiment, the intensity is a proxy measurement for the biofilm coverage in a given region.

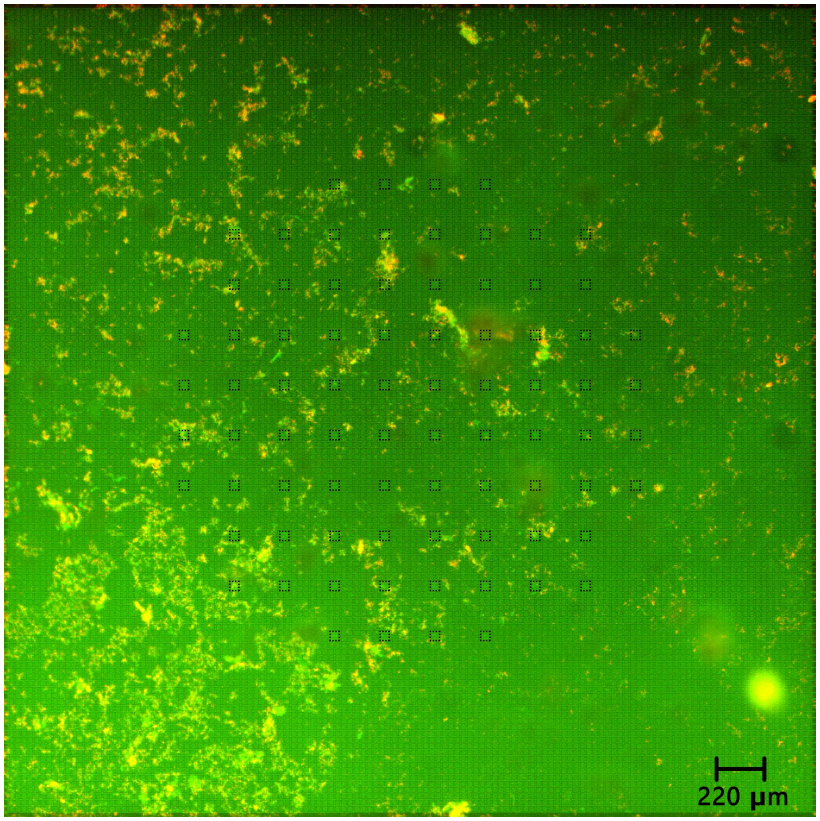

Figure 3.5: Chip Surface with Live (green) and Dead (red) Staining

The average green pixel intensities over each electrode region are computed, and then placed into two bins using a threshold in the middle - one bin with high intensity/coverage and one with low intensity/coverage. Using these, we can compare the resistance distributions of these two groups. As shown in Figure 3.6, the two distributions have different mean resistances (p=0.00088) as expected. The areas with higher coverage have also higher resistance as predicted which can be shown by a linear data fit.

Plotting the green pixel intensity ratio versus the measured resistance gives the result shown in Figure 3.7. This data shows the expected positive relation between the intensity and the resistance measured (p=0.000159) although the fluorescent measurements do have a fair amount of variance for this fit ($R^2 = 0.303$).

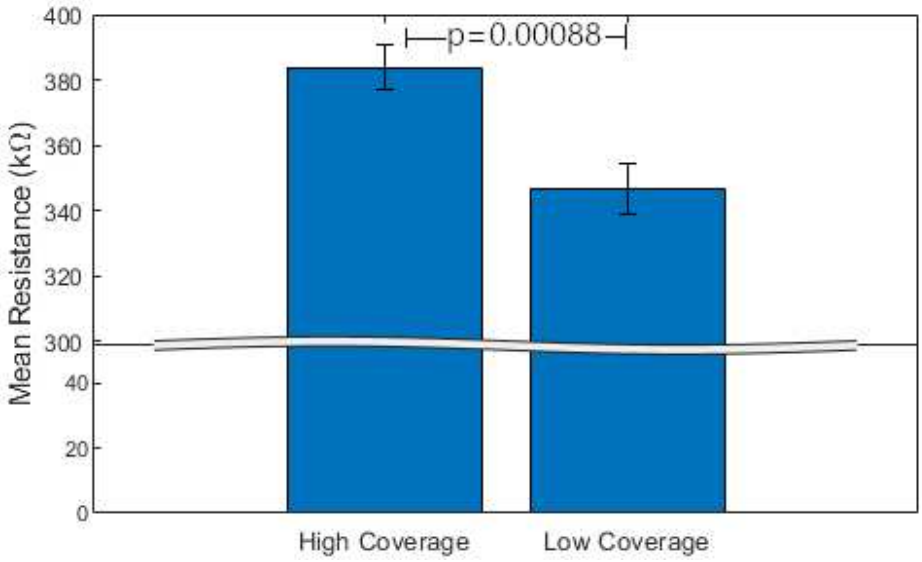

Figure 3.6: Resistance of Areas with High vs. Low Electrode Area Avg. Green Intensity

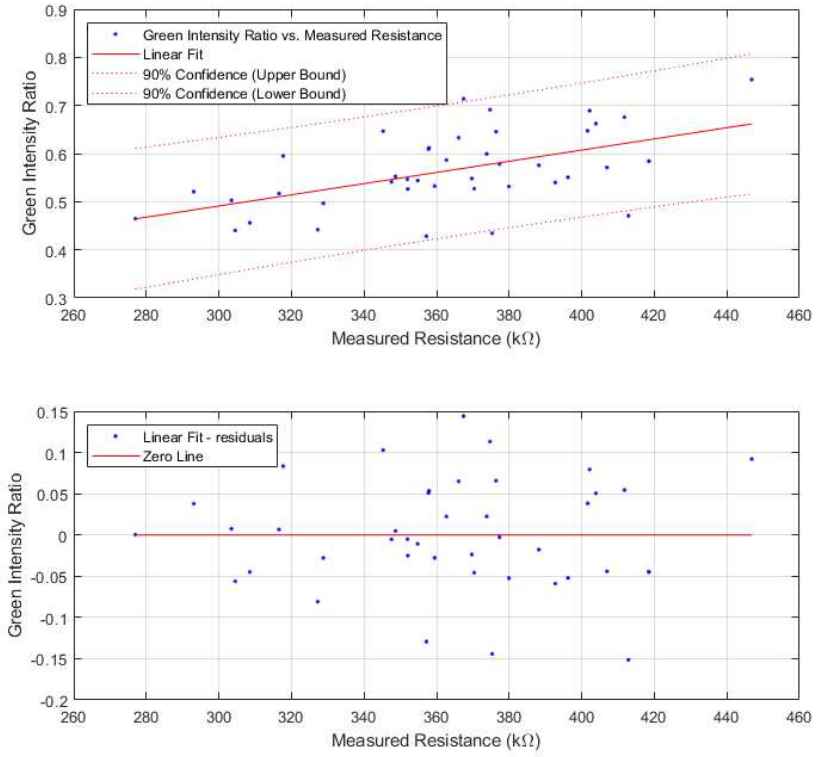

Figure 3.7: Electrode Area Avg. Intensity vs. Resistance (top) and Residuals (bottom)

Chapter 4

Conclusions and Future Work

The multi-channel impedance spectroscopy device successfully adds impedance sensing capabilities to the 3rd Gen CMOS biosensor platform, and opens the doors to many potential real-time spatial experiments. The coverage validation using florescence demonstrates the ability of the device to detect various levels of biofilm growth over the surface, and confirms a positive relation between biofilm occupancy and impedance modulus. The specification validation confirms that the device can operate over many of the ranges of EIS that have been used by previous experiments, and it broadens the capabilities allowing further quantitative analyses.

Future enhancements for this design include more gain variation in the front end to support a wider range of resistances, development of a standalone system with less expensive consumables, data logging, and some user interface improvements. However, the system currently is in a working state, and meets the needed specification ranges, so it is currently ready to be used for future studies in biofilm development.

Bibliography

[1] NIH, "RESEARCH ON MICROBIAL BIOFILMS," 2002.

[2] S. Veerachamy, T. Yarlagadda, G. Manivasagam, and P. KDV Yarlagadda, "Bacterial adherence and biofilm formation on medical implants: A review," *Journal of Engineering in Medicine*, vol. 228, no. 10, pp. 1083–1099, 2014.

[3] J. O'Neill, "Antimicrobial Resistance: Tackling a crisis for the health and wealth of nations," tech. rep., UK Review on Anti-Microbial Resistance, 2014.

[4] J. O'Neill, "Tackling Drug-Resistant Infections Globally: Final Report and Recommendations," tech. rep., UK Review on Anti-Microbial Resistance, 2016.

[5] M. Altaf, C. H. Miller, D. S. Bellows, and R. O'Toole, "Evaluation of the Mycobacterium smegmatis and BCG models for the discovery of Mycobacterium tuberculosis inhibitors," *Tuberculosis*, vol. 90, pp. 333–337, nov 2010.

[6] B. H. Neufeld, M. J. Neufeld, A. Lutzke, S. M. Schweickart, and M. M. Reynolds, "Metal–Organic Framework Material Inhibits Biofilm Formation of Pseudomonas aeruginosa," *Advanced Functional Materials*, vol. 27, no. 34, pp. 1–9, 2017.

[7] Q. Yu, E. F. Griffin, S. Moreau-Marquis, J. D. Schwartzman, B. A. Stanton, and G. A. O'toole, "In vitro evaluation of tobramycin and aztreonam versus Pseudomonas aeruginosa biofilms on cystic fibrosis-derived human airway epithelial cells," *Journal of Antimicrobial Chemotherapy*, vol. 67, no. 11, pp. 2673–2681, 2012.

[8] D. Nivens, R. Palmer Jr, and D. White, "Continuous nondestructive monitoring of microbial biofilms: a review of analytical techniques," *Journal of Industrial Microbiology*, vol. 15, no. 4, pp. 263–276, 1995.

[9] G. Chen, R. J. Palmer, and D. C. White, "Instrumental analysis of microbiologically influenced corrosion," *Biodegradation*, vol. 8, no. 3, pp. 189–200, 1997.

[10] Z. Keresztes, I. Felhősi, and E. Kálmán, "Role of redox properties of biofilms in corrosion processes," *Electrochimica Acta*, vol. 46, no. 24-25, pp. 3841–3849, 2001.

[11] A. Radu, S. Anastasova-Ivanova, B. Paczosa-Bator, M. Danielewski, J. Bobacka, A. Lewenstam, and D. Diamond, "Diagnostic of functionality of polymer membrane-based ion selective electrodes by impedance spectroscopy," *Analytical Methods*, vol. 2, no. 10, pp. 1490–1498, 2010.

[12] T. Kim, J. Kang, J.-H. Lee, and J. Yoon, "Influence of attached bacteria and biofilm on double-layer capacitance during biofilm monitoring by electrochemical impedance spectroscopy," *Water Research*, vol. 45, pp. 4615–4622, oct 2011.

[13] H. Ben-Yoav, A. Freeman, M. Sternheim, and Y. Shacham-Diamand, "An electrochemical impedance model for integrated bacterial biofilms," *Electrochimica Acta*, vol. 56, pp. 7780–7786, sep 2011.

[14] Y. Chen, C. C. Wong, T. S. Pui, R. Nadipalli, R. Weerasekera, J. Chandran, H. Yu, and A. R. Rahman, "CMOS high density electrical impedance biosensor array for tumor cell detection," *Sensors and Actuators B: Chemical*, vol. 173, pp. 903–907, oct 2012.

[15] C. Erbay, G. Yang, P. de Figueiredo, R. Sadr, C. Yu, and A. Han, "Three-dimensional porous carbon nanotube sponges for high-performance anodes of microbial fuel cells," *Journal of Power Sources*, vol. 298, pp. 177–183, dec 2015.

[16] A. ter Heijne, D. Liu, M. Sulonen, T. Sleutels, and F. Fabregat-Santiago, "Quantification of bio-anode capacitance in bioelectrochemical systems using Electrochemical Impedance Spectroscopy," *Journal of Power Sources*, vol. 400, pp. 533–538, oct 2018.

[17] X. Dominguez-Benetton, S. Sevda, K. Vanbroekhoven, and D. Pant, "The accurate use of impedance analysis for the study of microbial electrochemical systems," *Chemical Society Reviews*, vol. 41, pp. 7228–7246, oct 2012.

[18] C. Patel, S. Dunn, and P. Takhistov, "Combined Spectrophotometric-Electrochemical Impedance Imaging System for Biofilm Research," *Journal of Laboratory Automation*, vol. 10, no. 1, pp. 16–23, 2005.

[19] B. H. Liu, K.-L. Li, K.-L. Kang, W.-K. Huang, and J.-D. Liao, "In situ biosensing of the nanomechanical property and electrochemical spectroscopy of Streptococcus mutans-containing biofilms," *Journal of Physics D: Applied Physics*, vol. 46, no. 275401, 2013.

[20] A. J. Mason, X. Liu, and L. Li, "High-throughput impedance spectroscopy biosensor array chip," *Philosophical Transactions of the Royal Society A: Mathematical, Physical and Engineering Sciences*, vol. 372, no. 2012, 2014.

[21] M. Varshney and Y. Li, "Interdigitated array microelectrodes based impedance biosensors for detection of bacterial cells," *Biosensors and Bioelectronics*, vol. 24, pp. 2951–2960, jun 2009.

[22] L. Yang and R. Bashir, "Electrical/electrochemical impedance for rapid detection of foodborne pathogenic bacteria," *Biotechnology Advances*, vol. 26, pp. 135–150, mar 2008.

Appendix A

Circuit Diagrams

The following pages contain the circuit diagrams for the multi-channel impedance board, revision 1.2.

- Top Level (Figure A.1)
- USB Module (Figure A.2)
- FUN_GEN Module (Figure A.3)
- MUX_IN Module (Figure A.4)
- TIA Module (Figure A.5)
- BOARD_INTERFACE Module (Figure A.6)
- LEVEL_SHIFT Module (Figure A.7)
- PWR Module (Figure A.8)

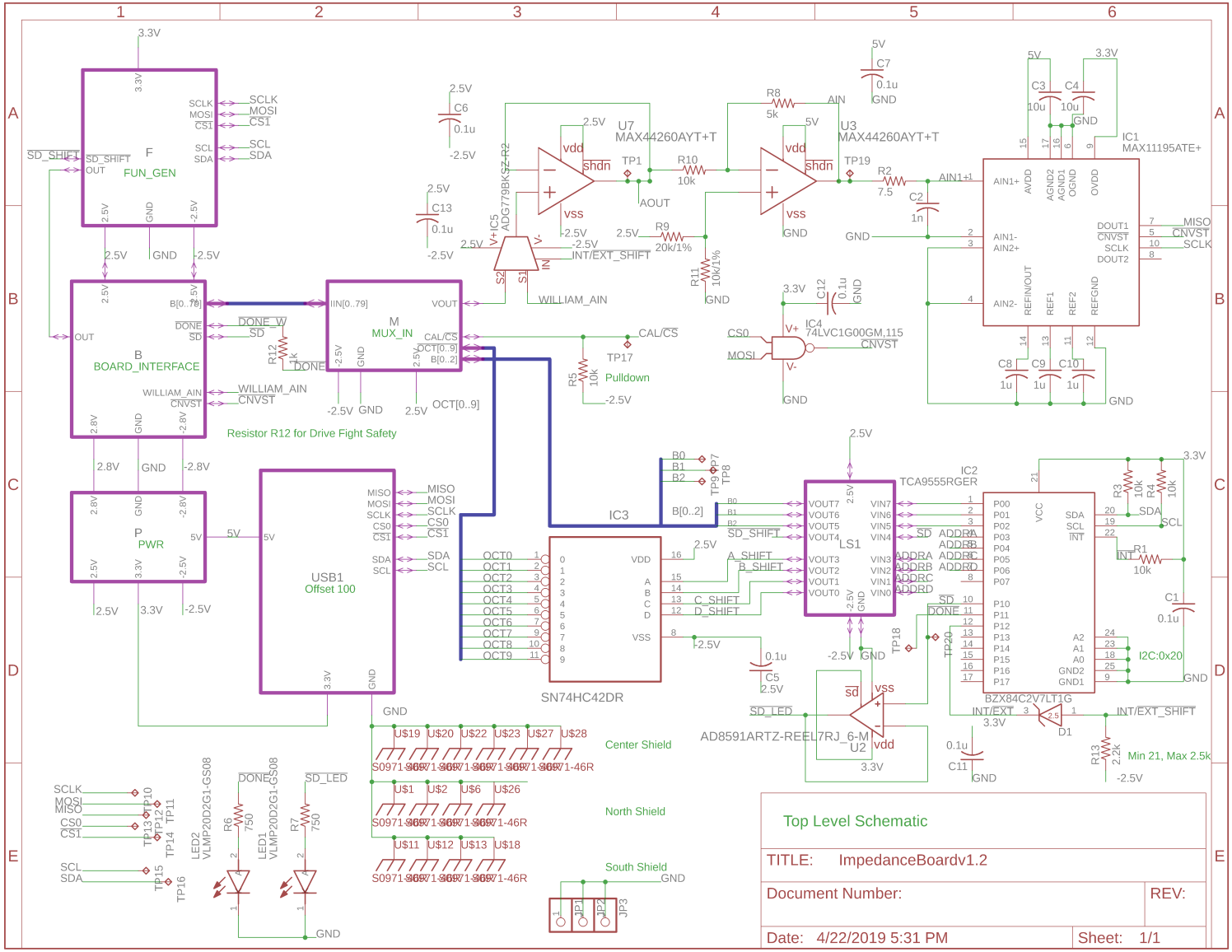

Figure A.1: Top-Level Circuit Diagram

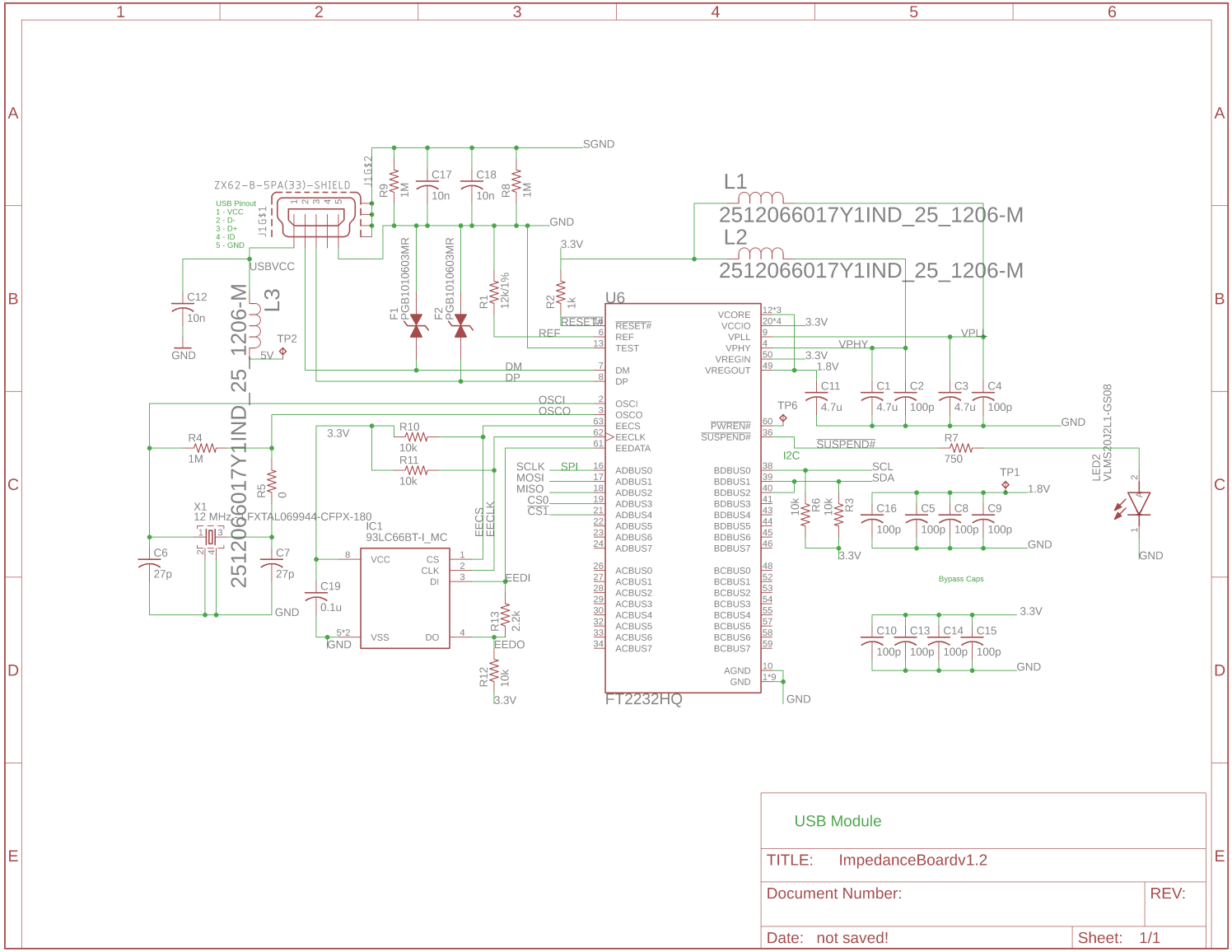

Figure A.2: USB Module Circuit Diagram

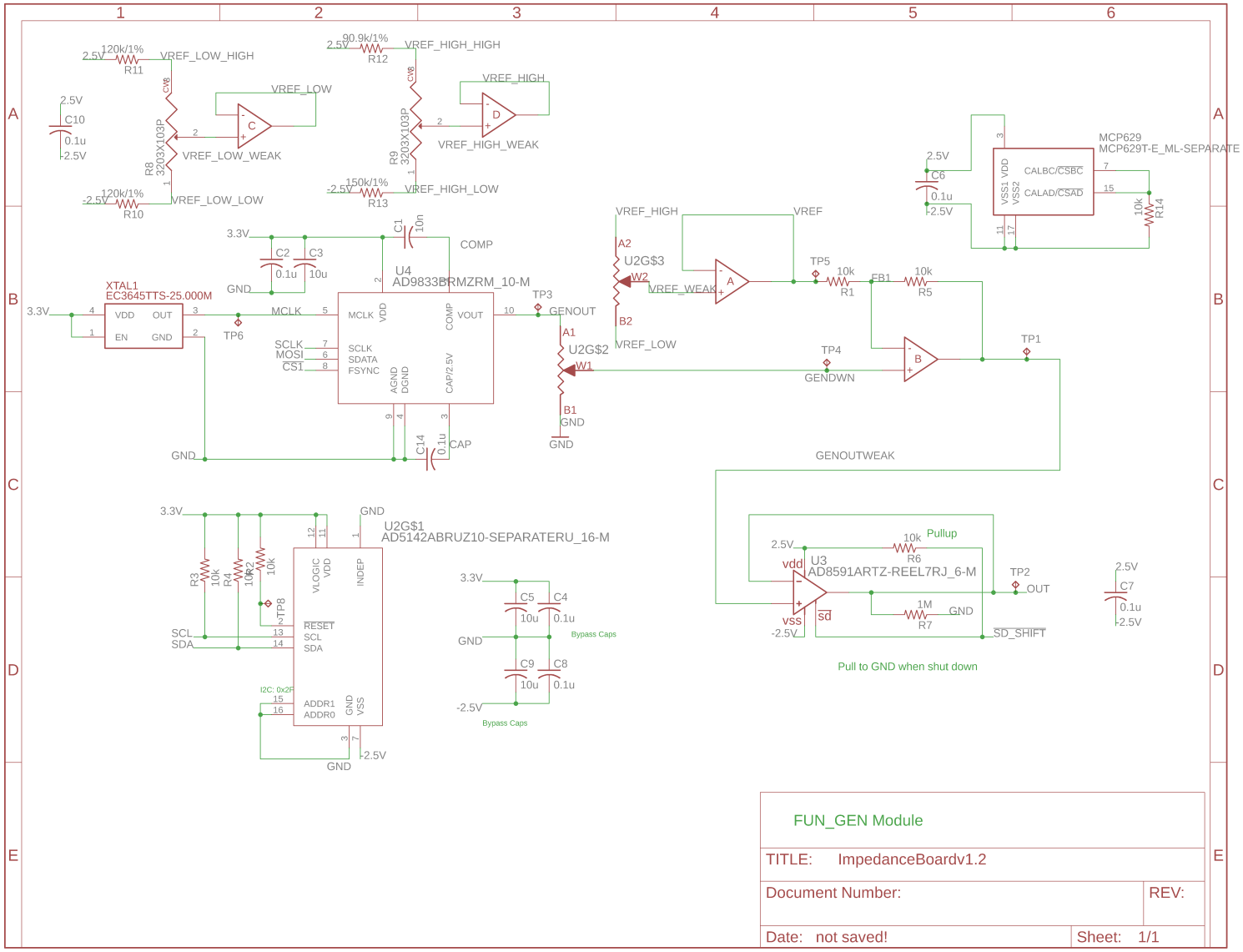

Figure A.3: Function Generation Module Circuit Diagram

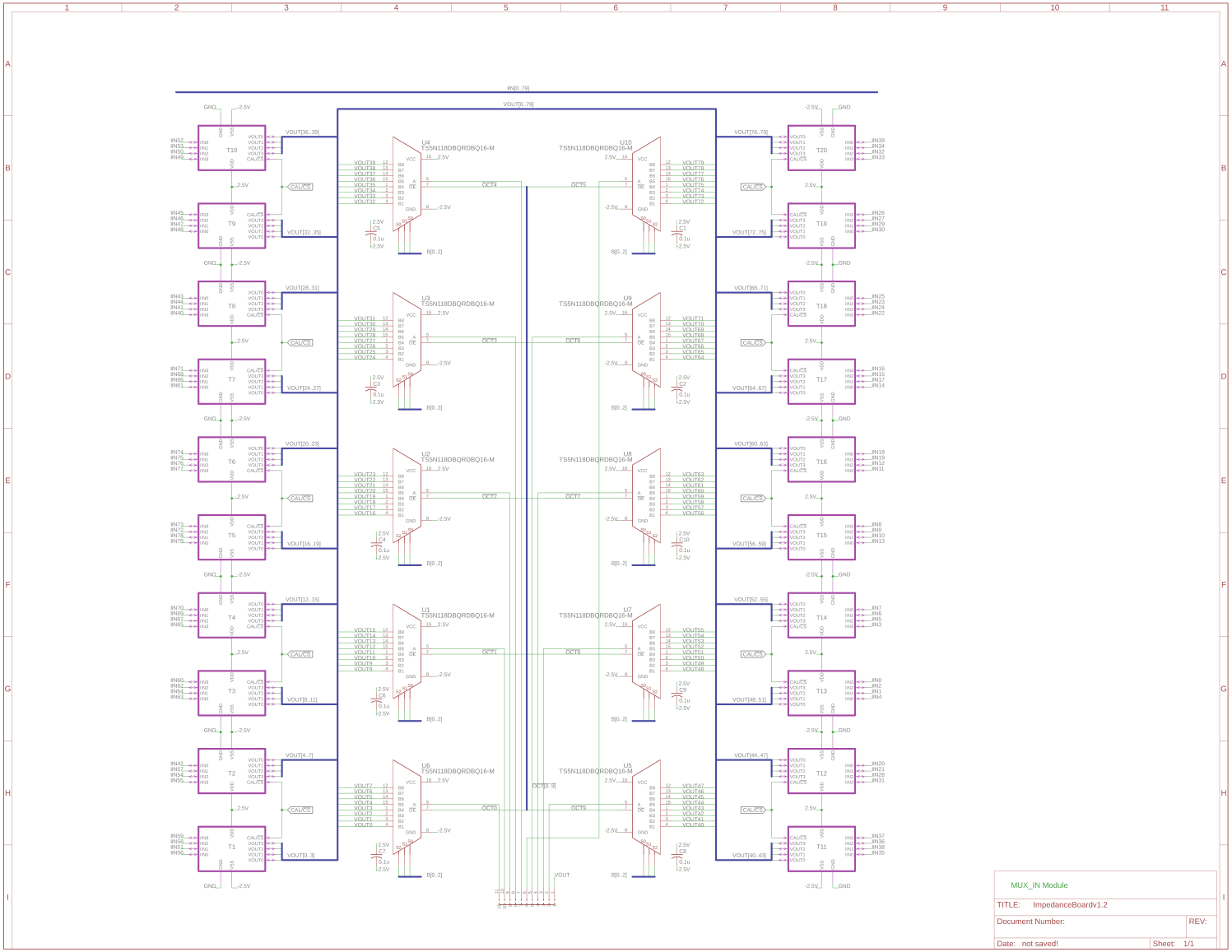

Figure A.4: MUX Module Circuit Diagram

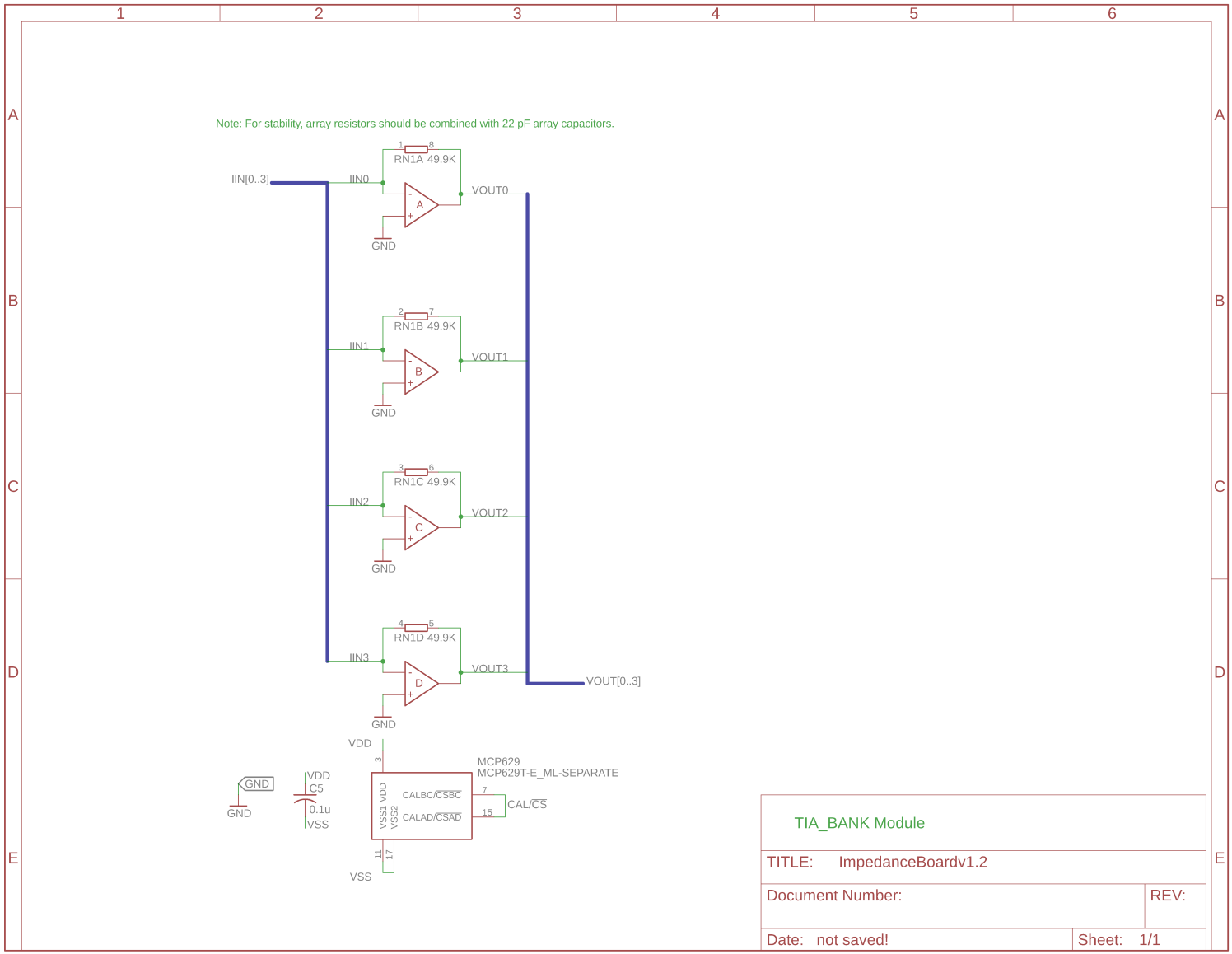

Figure A.5: Transimpedance Amplifier Module Circuit Diagram

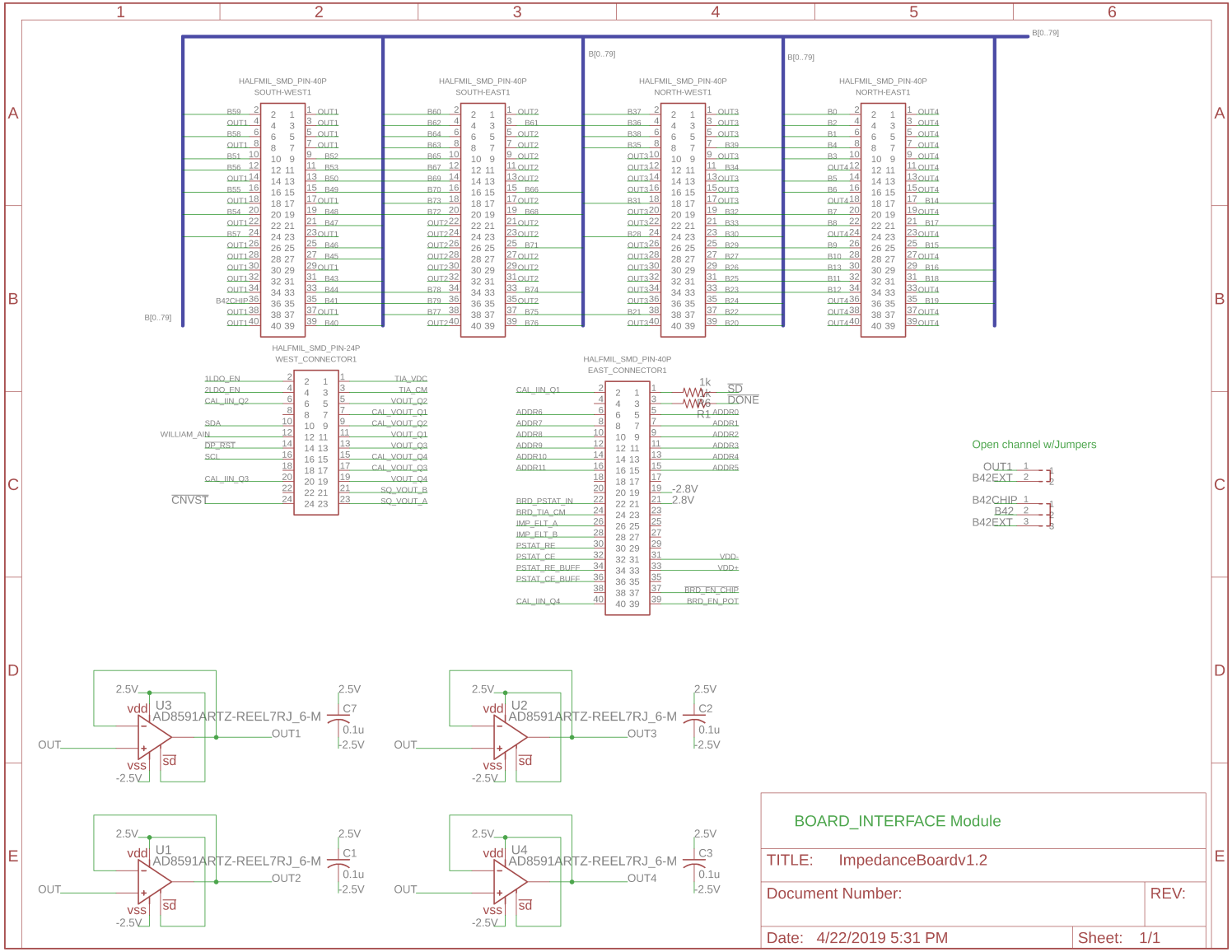

Figure A.6: Board Interface Module Circuit Diagram

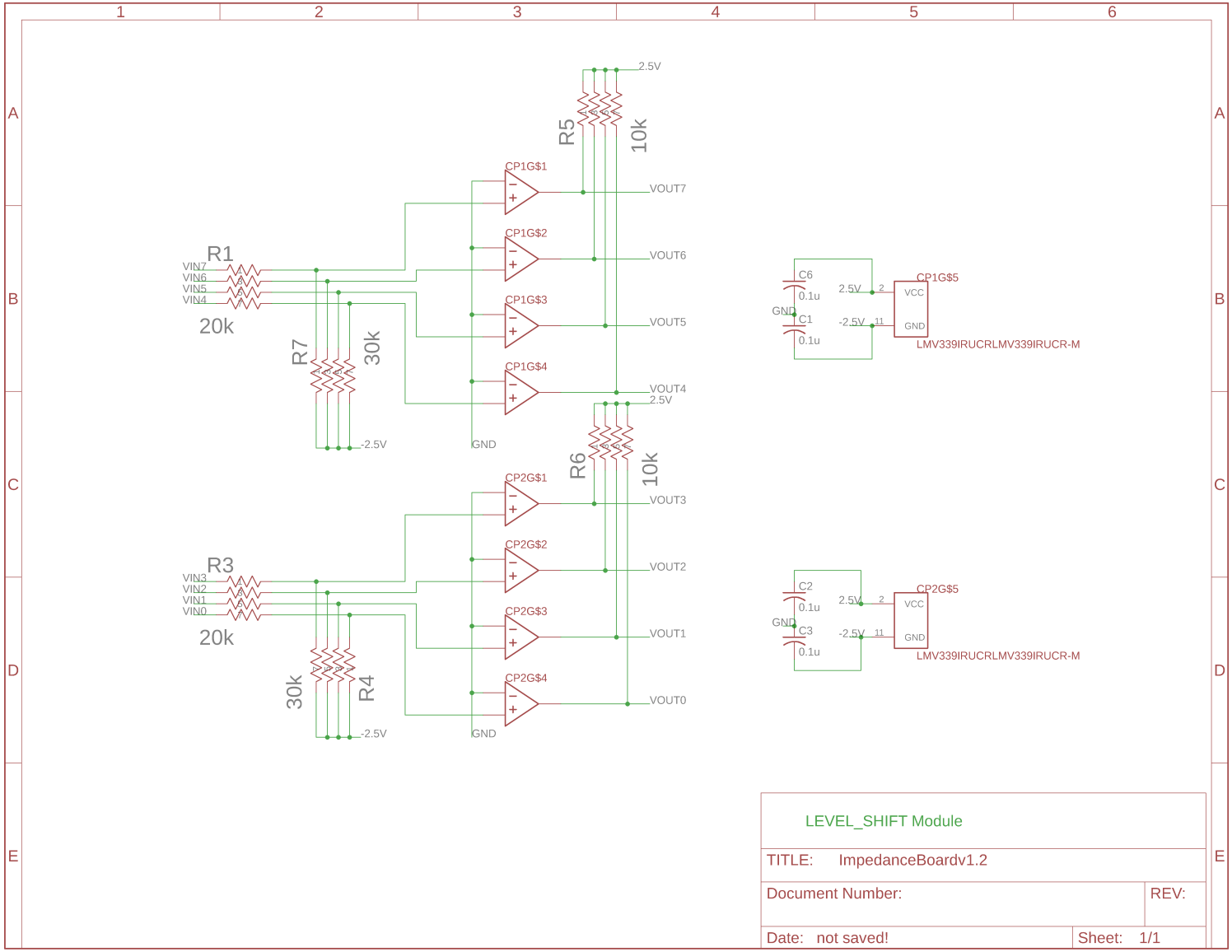

Figure A.7: Level Shift Module Circuit Diagram

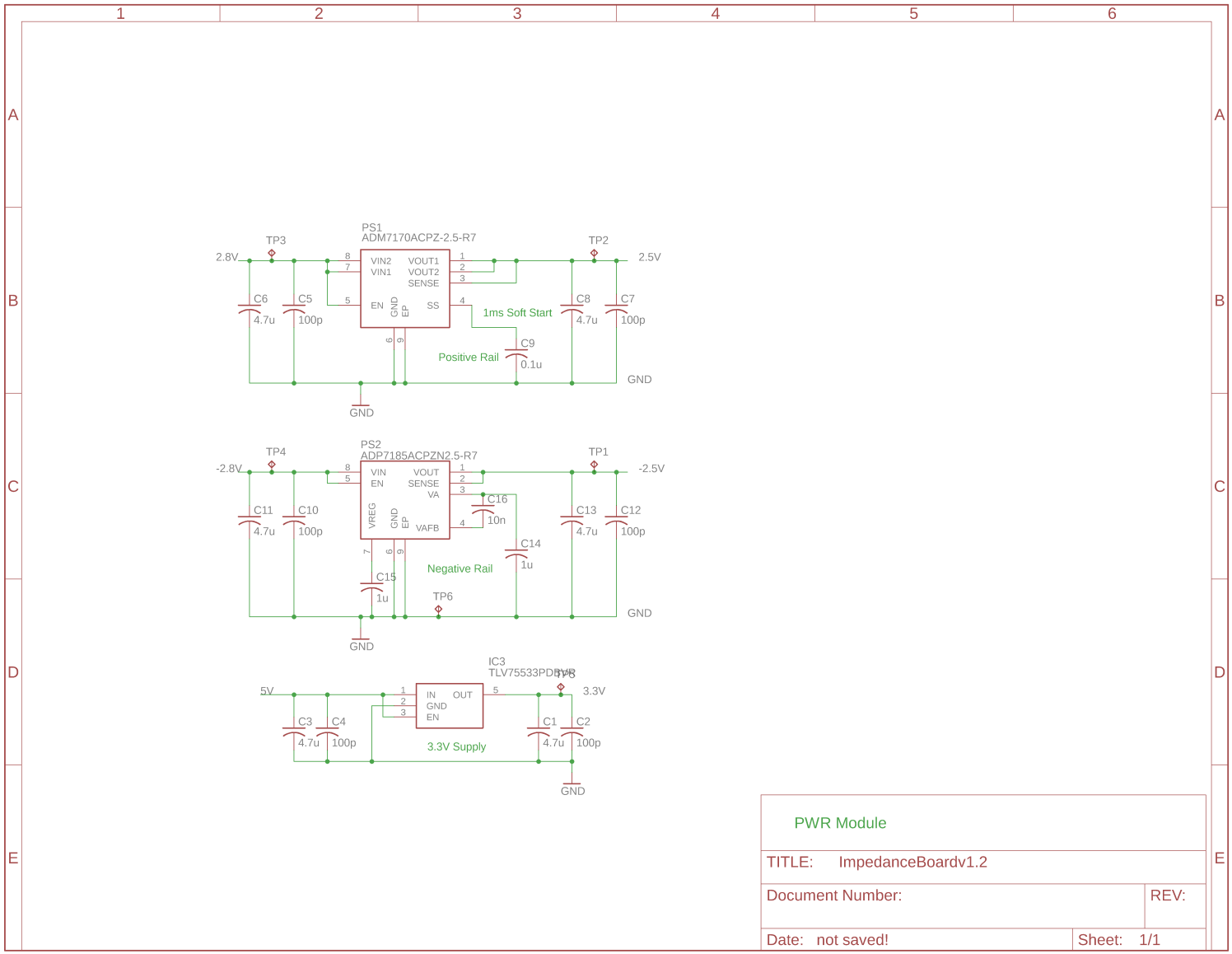

Figure A.8: Power Module Circuit Diagram

Appendix B

Bill of Materials

The following pages contain the bill of materials for the multi-channel impedance board revision 1.2. Total part cost for one system is $120.56. All prices are current as of April 30, 2019.

Table B.1: Bill of Materials

Qty	Part Description	Manufacturer Part #	Reference	Unit Price[6]	Ext. Price
1	1.27 mm Vertical Header, 24 Pin, Female	20021321-00024T4LF	B:WEST_CON1	$1.110	$1.110
1	1.27 mm Vertical Header, 24 Pin, Male	20021121-00024T4LF	B:WEST_CON1	$0.872	$0.872
5	1.27 mm Vertical Header, 40 Pin, Female	20021321-00040T4LF	B:EAST_CON1, B:NORTH-EAST1, B:NORTH-WEST1, B:SOUTH-EAST1, B:SOUTH-WEST1	$1.780	$8.900

Qty.	Part Description	Manufacturer Part #	Reference	Unit Price[7]	Ext. Price
5	1.27 mm Vertical Header, 40 Pin, Male	20021121-00040T4LF	B:EAST_CON1, B:NORTH-EAST1, B:NORTH-WEST1, B:SOUTH-EAST1, B:SOUTH-WEST1	$1.460	$7.300
1	12 MHz Quartz Crystal	LFXTAL069944	X101	$0.376	$0.376
1	2 Input NAND, 3.3V	74LVC1G00GM,115	IC4	$0.179	$0.179
3	2.5mm Header Pins, Male	Option	JP1, JP2, JP3	$0.003	$0.009
1	2.5V Zener Diode	BZX84C2V7LT1G	D1	$0.029	$0.029
1	2:1 Mux, 5.5V	ADG779BKSZ	IC5	$1.070	$1.070

Qty.	Part Description	Manufacturer Part #	Reference	Unit Price[7]	Ext. Price
10	8:1 Mux, 5V	TS5N118DBQR	M:U1, M:U2, M:U3, M:U4, M:U5, M:U6, M:U7, M:U8, M:U9, M:U10	$1.260	$12.600
1	ADC, 14 Bit, 2 MSPS	MAX11195ATE+	IC1	$5.100	$5.100
1	BCD Decoder	SN74HC42DR	IC3	$0.397	$0.397
5	C, 0603, 6.3V, 0.01μF	Option	C112, C117, C118, F:C1, P:C16	$0.011	$0.055

Qty.	Part Description	Manufacturer Part #	Reference	Unit Price[7]	Ext. Price
54	C, 0603, 6.3V, 0.1μF	Option	B:C1, B:C2, B:C3, B:C7, C1, C5, C6, C7, C11, C12, C13, C119, C201, C202, C203, C206, F:C2, F:C4, F:C6, F:C7, F:C8, F:C10, F:C14, M:C1, M:C2, M:C3, M:C4, M:C5, M:C6, M:C7, M:C8, M:C9, M:C10, M:T1:C5, M:T2:C5, M:T3:C5, M:T4:C5, M:T5:C5, M:T6:C5	$0.011	$0.594

Qty.	Part Description	Manufacturer Part #	Reference	Unit Price[7]	Ext. Price
	C, 0603, 6.3V, 0.1μF (continued)		M:T7:C5, M:T8:C5, M:T9:C5, M:T10:C5, M:T11:C5, M:T12:C5, M:T13:C5, M:T14:C5, M:T15:C5, M:T16:C5, M:T17:C5, M:T18:C5, M:T19:C5, M:T20:C5, P:C9		
5	C, 0603, 6.3V, 1μF	Option	C8, C9, C10, P:C14, P:C15	$0.012	$0.060
5	C, 0603, 6.3V, 10μF	Option	C3, C4, F:C3, F:C5, F:C9	$0.031	$0.155
1	C, 0603, 6.3V, 1000pF/1%	Option	C2	$0.024	$0.024

Qty.	Part Description	Manufacturer Part #	Reference	Unit Price[7]	Ext. Price
16	C, 0603, 6.3V, 100pF/1%	Option	C102, C104, C105, C108, C109, C110, C113, C114, C115, C116, P:C2, P:C4, P:C5, P:C7, P:C10, P:C12	$0.032	$0.512
2	C, 0603, 6.3V, 27pF/1%	Option	C106, C107	$0.039	$0.078
9	C, 0603, 6.3V, 4.7μF	Option	C101, C103, C111, P:C1, P:C3, P:C6, P:C8, P:C11, P:C13	$0.032	$0.288
20	Capacitor Array x4, 1206, 22pF/5%	W3A45A220J4T2A	Stack under M:T*:R*	$0.169	$3.38
1	CMOS Oscillator, 25MHz, 3.3V	EC3645TTS-25.000M	F:XTAL1	$0.660	$0.660

Qty.	Part Description	Manufacturer Part #	Reference	Unit Price[7]	Ext. Price
1	Digipot, 256 Positions	AD5142ABRUZ10	F:U2	$2.140	$2.140
1	Direct Digital Synthesis	AD9833BRMZ	F:U4	$5.240	$5.240
1	EEPROM 4K, 256x16	93LC66BT-I_MC	IC101	$0.300	$0.300
3	Ferrite Bead, 1206, 600Ω, 1A	2512066017Y1	L101, L102, L103	$0.034	$0.102
1	Fixed Output LDO, 2.5V, 0.5A	ADM7170ACPZ-2.5-R7	P:PS1	$1.190	$1.190
1	Fixed Output LDO, -2.5V, -0.5A	ADP7185ACPZN2.5-R7	P:PS2	$2.404	$2.404
1	Fixed Output LDO, 3.3V, 0.5A	TLV75533PDBVR	P:IC3	$0.268	$0.268
1	GPIO Interface	TCA9555RGER	IC2	$0.702	$0.702

Qty.	Part Description	Manufacturer Part #	Reference	Unit Price[7]	Ext. Price
2	Green LED, 1.8 V, 2 mA	VLMP20D2G1-GS08	LED1, LED2	$0.149	$0.298
2	Low Noise Op Amp	MAX44260AYT+T	U3, U7	$0.715	$1.430
6	Op Amp	AD8591ARTZ	B:U1, B:U2, B:U3, B:U4, F:U3, U2	$0.348	$2.088
1	Printed Circuit Board	Elecrow 4 Layer		$2.362	$2.362
2	Quad Comparator	LMV339IRUCR	CP201, CP202	$0.404	$0.808

Qty.	Part Description	Manufacturer Part #	Reference	Unit Price[7]	Ext. Price
21	Quad Op Amp, Low Offset	MCP629T-E_ML	F:IC1, M:T1:IC5, M:T2:IC5, M:T3:IC5, M:T4:IC5, M:T5:IC5, M:T6:IC5, M:T7:IC5, M:T8:IC5, M:T9:IC5, M:T10:IC5, M:T11:IC5, M:T12:IC5, M:T13:IC5, M:T14:IC5, M:T15:IC5, M:T16:IC5, M:T17:IC5, M:T18:IC5, M:T19:IC5, M:T20:IC5	$2.110	$44.310
1	R, 0603, 0Ω	Option	R105	$0.004	$0.004

Qty.	Part Description	Manufacturer Part #	Reference	Unit Price[7]	Ext. Price
18	R, 0603, 10kΩ/1%	Option	F:R1, F:R2, F:R3, F:R4, F:R5, F:R6, F:R14, R1, R3, R4, R5, R10, R11, R103, R106, R110, R111, R112	$0.005	$0.090
2	R, 0603, 120kΩ/1%	Option	F:R10, F:R11	$0.005	$0.010
1	R, 0603, 12kΩ/1%	Option	R101	$0.005	$0.005
1	R, 0603, 150kΩ/1%	Option	F:R13	$0.005	$0.005
4	R, 0603, 1kΩ/5%	Option	B:R1, B:R6, R12, R102	$0.004	$0.016
4	R, 0603, 1MΩ/5%	Option	F:R7, R104, R108, R109	$0.005	$0.020
2	R, 0603, 2.2kΩ/1%	Option	R13, R113	$0.005	$0.010
1	R, 0603, 20kΩ/1%	Option	R9	$0.005	$0.005
1	R, 0603, 4.99kΩ/1%	Option	R8	$0.005	$0.005

Qty.	Part Description	Manufacturer Part #	Reference	Unit Price[7]	Ext. Price
1	R, 0603, 7.5Ω/5%	Option	R2	$0.004	$0.004
3	R, 0603, 750Ω/5%	Option	R6, R7, R107	$0.005	$0.015
1	R, 0603, 90.9kΩ/1%	Option	F:R12	$0.083	$0.083
1	Red LED, 1.8 V, 2 mA	VLMS20J2L1-GS08	LED102	$0.115	$0.115
2	Resistor Array x4, 1206, 10kΩ/5%	YC164-JR-0710KL	R205, R206	$0.020	$0.040
2	Resistor Array x4, 1206, 20kΩ/5%	YC164-JR-0720KL	R201, R203	$0.020	$0.040
2	Resistor Array x4, 1206, 30kΩ/5%	YC164-JR-0730KL	R204, R207	$0.020	$0.040

Qty.	Part Description	Manufacturer Part #	Reference	Unit Price[7]	Ext. Price
20	Resistor Array x4, 1206, 49.9kΩ/1%	CAT16-4992F4LF	M:T1:RN1, M:T2:RN1, M:T3:RN1, M:T4:RN1, M:T5:RN1, M:T6:RN1, M:T7:RN1, M:T8:RN1, M:T9:RN1, M:T10:RN1, M:T11:RN1, M:T12:RN1, M:T13:RN1, M:T14:RN1, M:T15:RN1, M:T16:RN1, M:T17:RN1, M:T18:RN1, M:T19:RN1, M:T20:RN1	$0.177	$3.540

Qty.	Part Description	Manufacturer Part #	Reference	Unit Price[7]	Ext. Price
14	Shield Clip	S0971-46R	U$1, U$2, U$6, U$11, U$12, U$13, U$18, U$19, U$20, U$22, U$23, U$26, U$27, U$28	$0.159	$2.226
2	Trim Pot, 10kΩ	3203X103P	F:R8, F:R9	$1.160	$2.320
2	TVS Diode, 24V	PGB1010603MR	F101, F102	$0.239	$0.478
1	USB Interface/MPSSE	FT2232HQ	U106	$3.700	$3.700
1	USB Micro B Port	ZX62-B-5PA(33)	J101	$0.396	$0.396

[7]Unit price at 1000 units

Appendix C

Printed Circuit Board Design

The following pages contain the printed circuit board designs for the multi-channel impedance board revision 1.2 and calibration board.

- Top Layer (Figure C.1)
- Route 2 Inner Layer (Figure C.2)
- Route 15 Inner Layer (Figure C.3)
- Bottom Layer (Figure C.4)
- Calibration Board Top Layer (Figure C.5)
- Calibration Board Bottom Layer (Figure C.6)

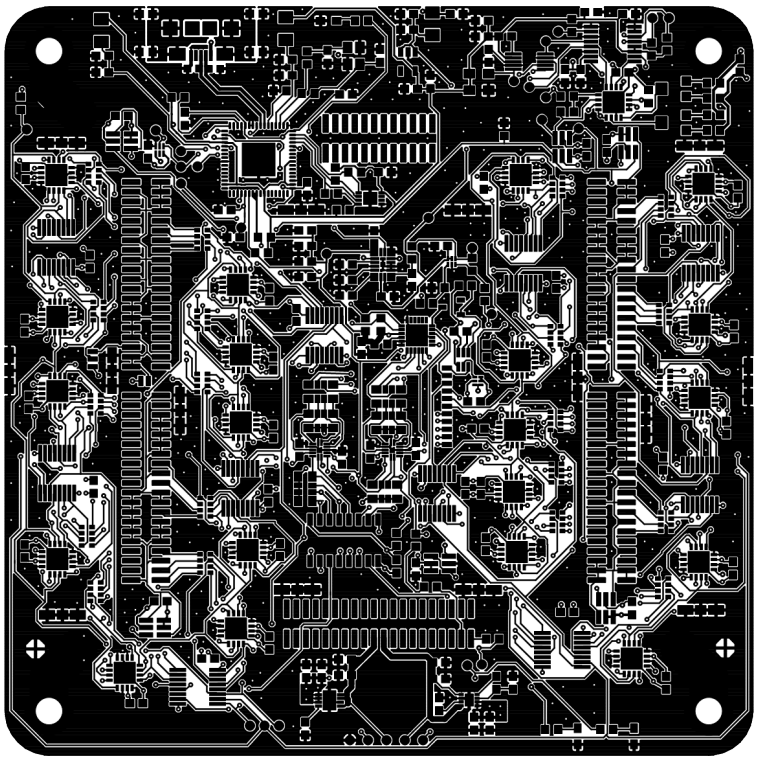

Figure C.1: Impedance Board v1.2 Top Layer

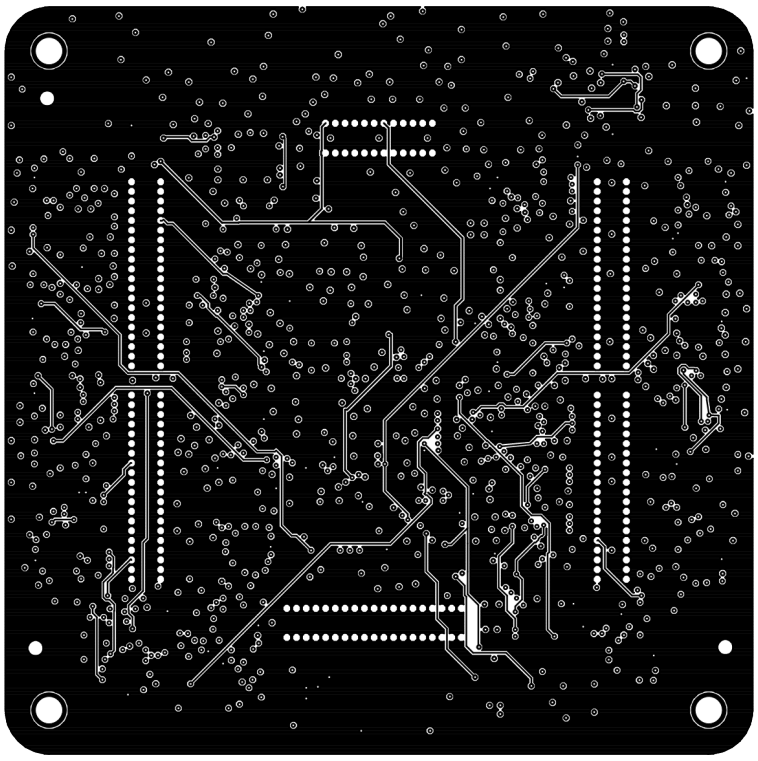

Figure C.2: Impedance Board v1.2 Route 2 Inner Layer

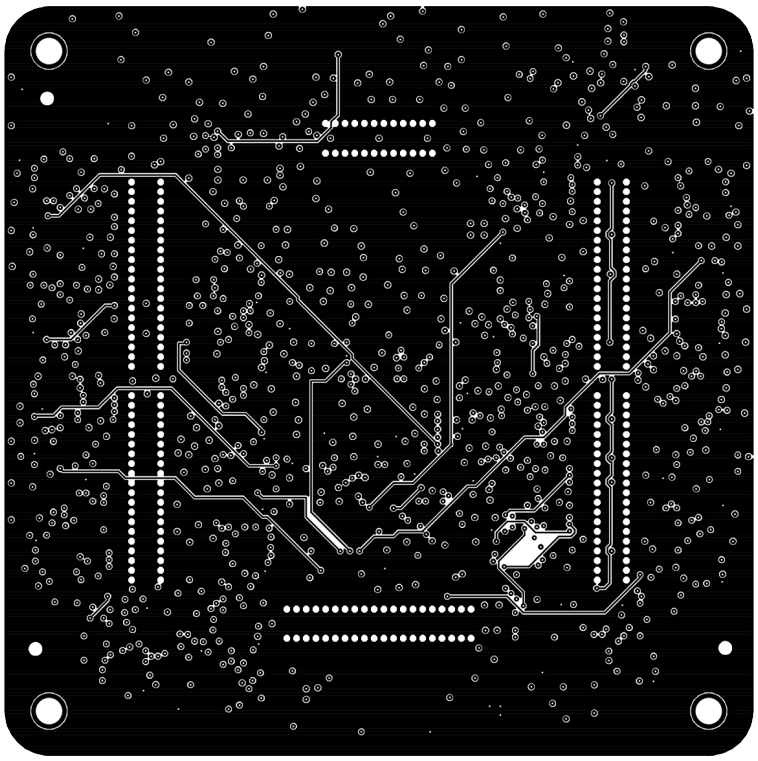

Figure C.3: Impedance Board v1.2 Route 15 Inner Layer

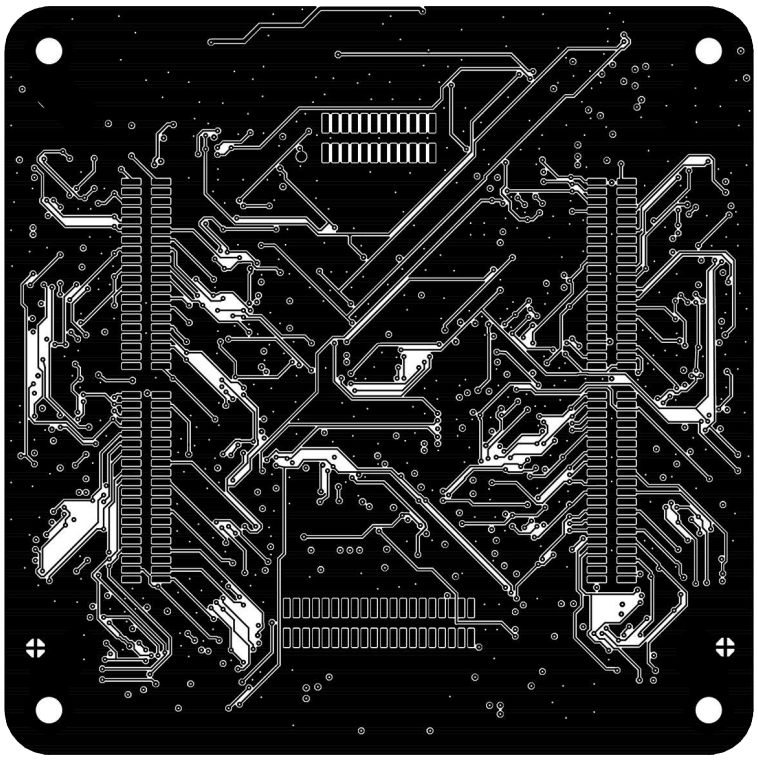

Figure C.4: Impedance Board v1.2 Bottom Layer

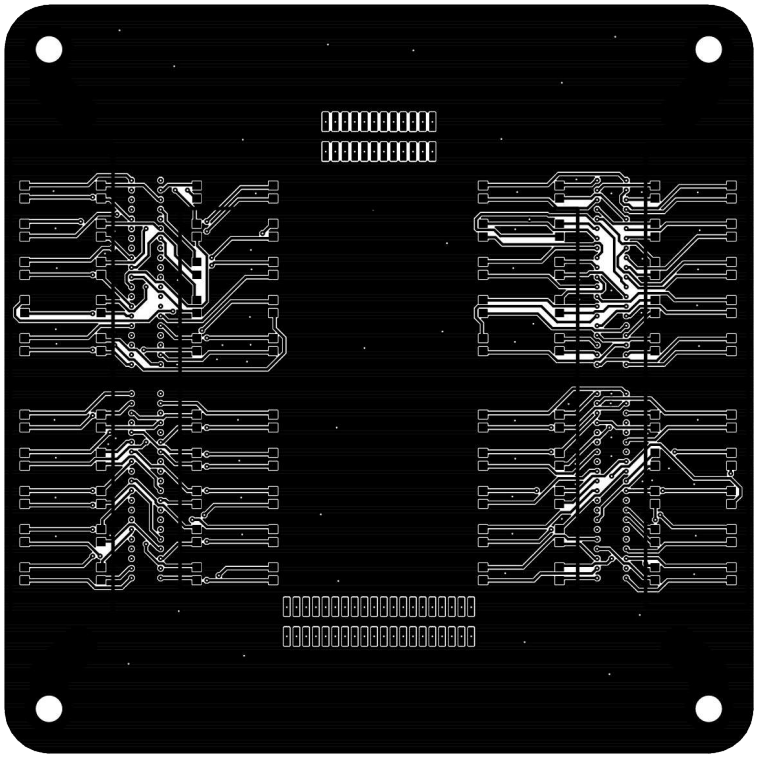

Figure C.5: Calibration Board v1.0 Top Layer

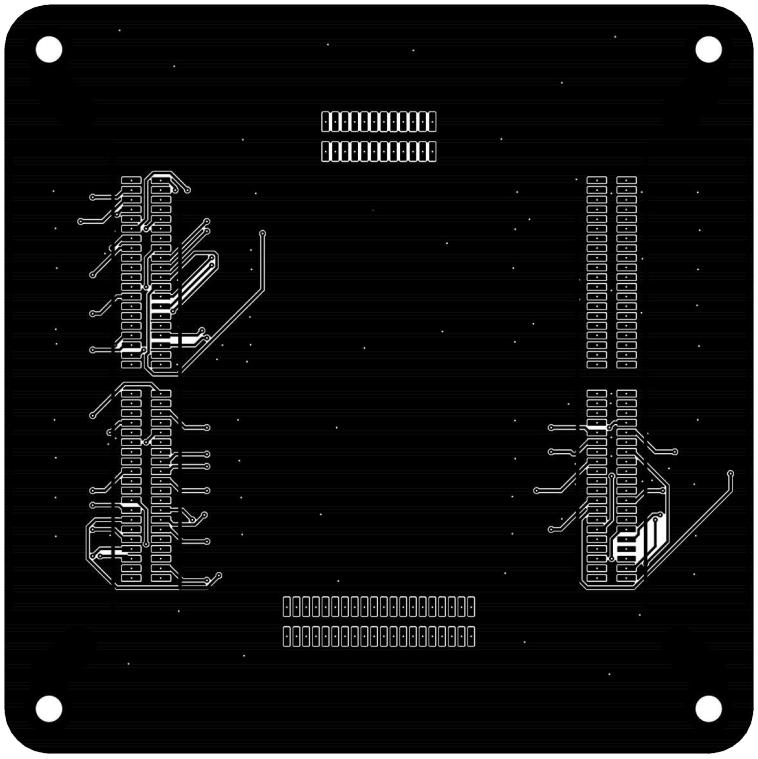

Figure C.6: Calibration Board v1.0 Bottom Layer

Appendix D

Least Squares Derivation

This appendix details the derivation of linear least squares from the definition of minimizing the residual sum of squares. It provides the motivation and method for performing LLS fitting using the Moore-Penrose pseudo inverse. This derivation was previously prepared for the Biomedical Signal Processing class.

Let

$$p = \text{Number of features in X (extracted features plus one)} \tag{D.1}$$

$$k = \text{Number of instances in X} \tag{D.2}$$

$$X = \text{Feature/instance matrix } (p \times k) \tag{D.3}$$

$$\vec{y} = \text{Known classifications/values related to X } (p \times 1) \tag{D.4}$$

$$\vec{\beta} = \text{vector of weights } \beta_0 ... \beta_p (p \times 1) \tag{D.5}$$

$$\boxdot^T = \text{transpose of } \boxdot \tag{D.6}$$

$$\hat{\boxdot} = \text{estimate of } \boxdot \tag{D.7}$$

$$\boxdot_{(i \times j)} = \text{The term } \boxdot \text{ has i rows and j columns} \tag{D.8}$$

Note that X has one feature that is all ones so it can weight the offset β_0. Using the estimates for beta, we want to find the estimates for y using:

$$\hat{\vec{y}}_{(k \times 1)} = X^T_{(k \times p)} \hat{\vec{\beta}}_{(p \times 1)} \tag{D.9}$$

We begin with the expression for the residual sum of squares (RSS) which we want to reduce, and convert it to matrix representation. This is the sum of squared error in the system, expressed as the sum over the k instances.

$$
\begin{aligned}
\text{RSS}(\beta) &= \sum_{i=1}^{k}(y_i - x_{i_{(1\times p)}}^T \vec{\beta}_{(p\times 1)})^2 \\
&= (\vec{y}_{(k\times 1)} - X_{(k\times p)}^T \vec{\beta}_{(p\times 1)})_{(1\times k)}^T (\vec{y}_{(k\times 1)} - X_{(k\times p)}^T \vec{\beta}_{(p\times 1)})_{(k\times 1)} \\
&= (\vec{y}_{(1\times k)}^T - (X_{(k\times p)}^T \vec{\beta}_{(p\times 1)})^T)_{(1\times k)} (\vec{y}_{(k\times 1)} - X_{(k\times p)}^T \vec{\beta}_{(p\times 1)})_{(k\times 1)} \\
&= (\vec{y}_{(1\times k)}^T - \vec{\beta}_{(1\times p)}^T X_{(p\times k)})_{(1\times k)} (\vec{y}_{(k\times 1)} - X_{(k\times p)}^T \vec{\beta}_{(p\times 1)})_{(k\times 1)} \\
&= \vec{y}_{(1\times k)}^T \vec{y}_{(k\times 1)} - \vec{y}_{(1\times k)}^T X_{(k\times p)}^T \vec{\beta}_{(p\times 1)} - \vec{\beta}_{(1\times p)}^T X_{(p\times k)} \vec{y}_{(k\times 1)} + \vec{\beta}_{(1\times p)}^T X_{(p\times k)} X_{(k\times p)}^T \vec{\beta}_{(p\times 1)}
\end{aligned}
\tag{D.10}
$$

To minimize this expression, we can take the gradient across all beta. Since each function of beta is quadratic (they are the square of the differences) there will be only one extremum - the minimum.

Using the gradient on the scalar RSS function will yield a column vector:

$$
\nabla_\beta = \begin{pmatrix} \dfrac{\partial(RSS)}{\partial\beta_0} \\ \dfrac{\partial(RSS)}{\partial\beta_1} \\ \vdots \\ \dfrac{\partial(RSS)}{\partial\beta_p} \end{pmatrix}
\tag{D.11}
$$

$$
\begin{aligned}
\nabla_\beta RSS &= \nabla_\beta (\vec{y}_{(1\times k)}^T \vec{y}_{(k\times 1)} - \vec{y}_{(1\times k)}^T X_{(k\times p)}^T \vec{\beta}_{(p\times 1)} \\
&\qquad - \vec{\beta}_{(1\times p)}^T X_{(p\times k)} \vec{y}_{(k\times 1)} + \vec{\beta}_{(1\times p)}^T X_{(p\times k)} X_{(k\times p)}^T \vec{\beta}_{(p\times 1)}) \\
&= \vec{0}_{(p\times 1)} - (\vec{y}_{(1\times k)}^T X_{(k\times p)}^T)_{(p\times 1)}^T - X_{(p\times k)} \vec{y}_{(k\times 1)} + 2X_{(p\times k)} X_{(k\times p)}^T \vec{\beta}_{(p\times 1)} \\
&= -2X_{(p\times k)} \vec{y}_{(k\times 1)} + 2X_{(p\times k)} X_{(k\times p)}^T \vec{\beta}_{(p\times 1)}
\end{aligned}
\tag{D.12}
$$

Setting the gradient equal to a zero vector and solving for beta will yield the beta estimate that has the minimum sum of squares, since that solves the system of equations for the minimum in each beta dimension.

$$\begin{aligned}
\nabla_\beta RSS = \vec{0}_{(p\times 1)} &= -2X_{(p\times k)}\vec{y}_{(k\times 1)} + 2X_{(p\times k)}X^T_{(k\times p)}\hat{\vec{\beta}}_{(p\times 1)} \\
-2X_{(p\times k)}X^T_{(k\times p)}\hat{\vec{\beta}}_{(p\times 1)} &= -2X_{(p\times k)}\vec{y}_{(k\times 1)} \\
X_{(p\times k)}X^T_{(k\times p)}\hat{\vec{\beta}}_{(p\times 1)} &= X_{(p\times k)}\vec{y}_{(k\times 1)} \\
\hat{\tilde{\beta}}_{(\mathbf{p\times 1})} &= (\mathbf{X_{(p\times k)}X^T_{(k\times p)}})^{-1}\mathbf{X_{(p\times k)}\tilde{y}_{(k\times 1)}}
\end{aligned} \tag{D.13}$$

Thus we get the expression $\hat{\tilde{\beta}} = (\mathbf{XX^T})^{-1}\mathbf{X\tilde{y}}$. Also note that if X is defined in the opposite way (where $\tilde{X} = X^T$) then we get the equivalent statement $\vec{\beta} = (\tilde{X}^T\tilde{X})^{-1}\tilde{X}^T\vec{y}$.